Accepted Manuscript

Study on fatigue life of bend-twist coupling wind turbine blade based on anisotropic beam model and stress-based fatigue analysis method

Hang Meng, Fue-Sang Lien, Gregory Glinka, Paul Geiger

# Study on fatigue life of bend-twist coupling wind turbine blade based on anisotropic beam model and stress-based fatigue analysis method

Hang Meng[a,*], Fue-Sang Lien[a,b], Gregory Glinka[a], Paul Geiger[a]

[a]*Department of Mechanical and Mechatronics Engineering, University of Waterloo, Waterloo, Ontario, N2L 3G1, Canada*
[b]*Key Laboratory of Metallurgical Equipment and Control Technology of Ministry of Education, Wuhan University of Science and Technology, Wuhan, Hubei, 430081, China*

## Abstract

Bend-twist coupling (BTC), also called aeroelastic tailoring or passive pitch control method, is often utilized to reduce the fatigue loading on wind turbine blades. With BTC, the blade can twist as it bends, this alleviates the aerodynamic force due to the decrease in the angle of attack when the load is increased suddenly. In this research, the stress-based method is employed to investigate the fatigue load due to the BTC effect under different wake conditions. To begin with, the one-dimensional anisotropic beam model is adopted in aeroelastic simulation. Next the static and modal analyses for the NREL 5MW wind turbine blade with different fiber orientations are performed to verify the anisotropic beam model. Finally, the stress history of each element on each cross section is reconstructed using DTU BECAS. The fatigue life of different materials in each cross section under different wake conditions has been analysed. The results show that the predicted fatigue life of NREL 5MW wind turbine blade (26.0187 years) is very close to the design life (20 years). The fatigue effect has an impact on the life of wind turbine blades, which can be affected by the layout of wind turbines and alleviated by BTC effect.

*Keywords:* wind turbine fatigue, bend-twist coupling, aero-elasticity, stress life fatigue analysis

## 1. Introduction

The fatigue damage of wind turbine blades, which are constructed from composite materials, is driven by the ambient flow and wake operations. The fatigue damage threatens the safety and stability of the wind turbine structure and thus lowers the economy and efficiency of the power generation system. It is also a bottle-neck for increasing the length of wind turbine blade to achieve higher efficiency [1]. As a result, the fatigue load mitigation method attracts attentions from both wind energy industry and academic researchers. Nowadays, two methods are often utilised to mitigate the fatigue load, the active and passive pitch control methods [2]. With the active pitch control method, the unsteady aerodynamic loading is controlled actively by additional control devices, such as moving surface in the trailing edge [3]. In contrast to the active control method, the passive control takes advantage of bend-twist coupling (BTC) effect of composite materials, which means that this kind of blade can twist as it bends. Taking advantage of the BTC effect, the instant loading can be reduced due to the change in the angle of attack [4].

This BTC concept stems from aeronautical industry, and it has been successfully used in the design of F-86 Sabre and the Boeing B-47 Stratojet to mitigate the aerodynamic load (see the page 9 of [5]). In the modern wind energy industry, nowadays, there are two main branches of BTC concepts: "twist-to-stall" and "twist-to-feather". As for the "twist-to-stall" wind turbine blade, the blade tends to operate in the stall region to reduce the load during instant wind speed increase. However, this BTC technique makes the blade suffer from flutter instability [6] and a substantial fatigue damage. In fact, the "twist-to-stall" design is always adopted to capture more energy rather than to reduce the fatigue damage [7]. Instead of increasing the angle of attack to the stall region, the "twist-to-feather" blade is

---

*Corresponding author
    Email address:* windsimu@gmail.com (Hang Meng)

17 designed to decrease the angle of attack when the wind speed suddenly increases. Recent research concentrates on BTC with "twist-to-

18 feather" because of its quick response to gusts and effective fatigue load mitigation [4]. The flutter instability and fatigue increase issue

19 in "twist-to-stall" design are not obvious in BTC with "twist-to-feather" design. Although there is no application of BTC concept in the

20 design of large off-shore wind turbine blades (e.g. 5MW wind turbine blades), the BTC design still has a potential to provide a solution

21 to the fatigue mitigation of large wind turbines, especially for off-shore wind turbines. As a result, in this paper, the "twist-to-feather"

22 BTC blade will be studied and discussed.

23 In the area of "twist-to-feather" BTC blades, previous research mainly focused on the static analysis or dynamic analysis of cyclic

24 load [8, 9] of BTC blades based on 3D fully-blade-resolved FEM analysis to achieve higher coupling coefficient. However, for fatigue

25 analysis, aeroelasticity of a wind turbine is also a dominant factor so that the governing equations of flow part and structural part should

26 be coupled and solved together [10]. Due to its large computational cost, the 3D fully-blade-resolved method is less attractive to the

27 researchers and engineers who study multiple wind turbines. Moreover, the fatigue analysis of wind turbine blades requires large amount

28 of loading time series, which further increases the computational cost. Although there exists the spectrum method, in which the loading

29 can be generated by using an empirical model, such as WISPERX spectrum [11], these methods are highly dependent on the structure of

30 wind turbine blades and wind turbulence. Due to the changes in the structures of the blade and wind conditions (e.g. wake conditions),

31 the nature of the spectrum will also change. As a result, an efficient aeroelastic model for BTC blades is required to generate loading time

32 series. The models based on beam theory are popular in the aeroelastic models of wind turbine blades [10]. The idea of the beam theory

33 is to split the 3D beam structure problem into a 2D cross-sectional analysis problem and a 1D beam modelling problem [12]. As for the

34 2D cross-sectional analysis problem, the previous models always assume that the beam is made of homogeneous and isotropic materials.

35 These models fail to simulate the anisotropic effects and warping effects caused by the composite materials (e.g. the bend-twist coupling

36 induced by the fibre orientations). To overcome these problems, Giavotto et al. proposed a 2D FEM method to compute the generalized

37 warping functions and cross-sectional properties for the beam structures [13]. Based on this theory, the DTU BECAS was developed

38 to analyse the cross-sectional properties of a wind turbine blade. For the 1D beam modelling, Kim et al [14] proposed the anisotropic

39 beam model on the basis of the aforementioned generalized 2D FEM cross-sectional analysis. In the present study, the DTU BECAS

40 (generalized 2D cross-sectional analysis tool) and the anisotropic beam model will be used to generate the dynamic loading of wind

41 turbine blades for fatigue analysis.

42 The moment-based fatigue analysis methods are popular in the wind energy industry, because of the utilization of aforementioned

43 beam models and empirical load spectrum. It is convenient to provide root bending moments (highest bending moment along the blade)

44 from beam models and empirical load spectrum rather than to provide the stress time series. As for the moment based method, the root

45 bending moments, including flapwise and edgewise bending moments, will be used to calculate the Damage Equivalent Load (DEL)

46 based on an M-N curve and rainflow counting algorithm according to the reference number of load ranges [15, 16, 17, 18]. Due to its

47 simplicity and robustness, it is now also adopted in the recent research of bend twist coupling wind turbine blades [4]. However, in this

48 method, the fatigue damage of different materials at a blade section cannot be calculated, which is also critical for bend-twist coupling

49 turbine blade design. In order to show the fatigue life of different materials at different cross sections under different wake conditions,

50 the stress-life method is used here.

51 Wind turbine blade is a kind of thin wall composite beam structure. For this kind of structure, there are three major methods for

52 fatigue life prediction, including macroscopic models (fatigue life models or empirical models), phenomenological models (stiffness or

53 strength degradation method), and progressive damage models. These three methods have been introduced comprehensively in [19]. The

54 first category of fatigue life models is based on the S-N curves and Constant Life Diagrams (CLD). The fatigue damage is calculated

55 by the empirical damage accumulation rules such as the Palmgren-Miner rule. The damage mechanism is not considered in this model.

56 Contrary to the aforementioned empirical fatigue life models, the second category of models capture the physics of fatigue damage

57 by introducing the fatigue metric of residual strength or residual stiffness. The fatigue failure occurs when the certain limit of fatigue

58 metric is reached. Despite the phenomenological models capturing the physical meaning of fatigue damage, it does not show better

59 performance compared with the first category of empirical models in the case of variable amplitude loading which is presented in [20]. In

60 the authors' view, this is caused by the complicated mechanism in fatigue damage of wind turbine blades. Therefore, further corrections

61 and improvements are also required for phenomenological models. The guidelines for safety factors of phenomenological models are

62 also lacking. The main disadvantage of these two aforementioned methods is that they are limited to the uniaxial loading cases and do

63 not take into account other stress components for fatigue life prediction. But they are reasonable for slender beam structures, such as

64 wind turbine blades, in which the normal stress in the beam axial direction is dominant. To deal with the complex loading patterns, the

65 third category of models, the progressive damage models, have been proposed based on micro mechanics, in this model, one or more

66 fatigue damage variables related to the observable damage mechanisms are introduced to model the damage modes, such as transverse

67 matrix cracks and de-laminations. Although this method is the most promising way to predict the fatigue life of composite structures, it

68 is still computationally intensive. Few authors have applied this method in the fatigue life prediction of wind turbine blades. As a result,

69 the first category of fatigue life models, which is also suggested in the GL guidelines for wind turbines, are adopted here to analyse the

70 longevity of the different materials of wind turbine blades. The stress time series are reconstructed through the use of DTU BECAS. The

71 novelty of this paper is to propose a fatigue analysis methodology based on the anisotropic beam model, cross sectional analysis model,

72 and fatigue analysis method for BTC wind turbine blade and the study of BTC effect under the wake conditions.

73 In this research paper, an anisotropic beam model based on the finite-element formulation [14] is used to model the macroscopic

74 motion of wind turbine blade including bending and torsion. Then, using two-dimensional sectional analysis code, BECAS [21], the

75 time series of stress on different blade sections are reconstructed according to the force and moment resultant time series from the

76 aforementioned anisotropic one-dimensional beam model, and the fatigue critical section (10.25 m from root) is determined. Lastly, the

77 fatigue analysis is carried out to investigate the bend-twist coupling effect on different composite materials on the each blade section.

78 The main body of this paper can be divided into three sections. In the first section, the methodology will be briefly introduced in

79 terms of the cross section model, beam model, aeroelastic model, and fatigue analysis method. In the second section, the results of the

80 static analysis and modal analysis of the NREL 5MW turbine blade will be presented. In the last section, the fatigue mitigation effects

81 of a BTC blade under ambient turbulence and wake turbulence conditions are demonstrated and discussed.

## 2. Methodology

83 Wind turbine blades are commonly assumed to be cantilever thin-walled beam. This assumption simplifies the structural modelling.

84 Concerning the computational efficiency, the blade element momentum method (BEM) is used in the present paper as the aerodynamic

85 model.

86 The BEM model and anisotropic beam model are coupled together in two ways. The BEM model provides the beam model with

87 the external aerodynamic forces (axial force and tangential force) at each cross section. In addition, the external forces cause the blade

88 to vibrate. The vibration-induced velocity (along the flapwise and edgewise directions) at each section will also affect the aerodynamic

89 force calculation of BEM in terms of the local inflow angle. In addition, the torsion of the blade induced by BTC will lead to a change

90 in the twist angle, which will also be considered in this model. The flowchart of this two-way coupling methodology is shown in Fig. 1.

91 The basic theories and equations in Fig. 1 will be further explained in this section.

92 The aforementioned anisotropic beam model is able to be coupled with more advanced aerodynamic models than the BEM model,

93 such as the actuator line model. For the fatigue analysis, according to GL certification [22], the stress-based analysis method is employed

3

94 and introduced in the last part in this section.

95 *2.1. Two-dimensional sectional analysis*

96 The BECAS model for 2D sectional analysis is presented here-in. This analysis is the basis of stiffness matrix construction (Equation

97 (5)) and stress reconstruction (Equation (7)).

98 The displacement of a point on a cross section can be represented by the following formula [14]

$$\mathbf{s} = \mathbf{v} + \mathbf{g} \tag{1}$$

99 In Equation (1), $\mathbf{s}$ is the vector of displacement; $\mathbf{v}$ is the vector associated with rigid body motion (rotation and translation); $\mathbf{g}$ is the

100 warping displacement vector which is generally neglected in the ad hoc beam models, such as Euler Bernoulli and Timoshenko beam

101 model. The detailed derivation of the cross sectional model can be found in [21] and is only briefly introduced in this section.

102 The governing equation of the cross-sectional displacement can be assumed to be a linear and homogeneous differential equations.

103 If the finite element formulation is employed, the relationship between the nodal warping displacement $\mathbf{U}$, generalized strain $\boldsymbol{\Phi}$ and the

104 external resultant $\boldsymbol{\theta}$ (six degrees of freedom) can be represented by the following equations [23]:

$$
\begin{aligned}
\mathbf{U}_{(n_d \times 1)} &= \mathbf{X}_{(n_d \times 6)} \boldsymbol{\theta}_{(6 \times 1)} & \boldsymbol{\Phi}_{(6 \times 1)} &= \mathbf{Y}_{(6 \times 6)} \boldsymbol{\theta}_{(6 \times 1)} \\
\frac{\partial \mathbf{U}}{\partial z}_{(n_d \times 1)} &= \frac{\partial \mathbf{X}}{\partial z}_{(n_d \times 6)} \boldsymbol{\theta}_{(6 \times 1)} & \frac{\partial \boldsymbol{\Phi}}{\partial z}_{(6 \times 1)} &= \frac{\partial \mathbf{Y}}{\partial z}_{(6 \times 6)} \boldsymbol{\theta}_{(6 \times 1)}
\end{aligned}
\tag{2}
$$

105 The critical variables in Equation (2) can be obtained by solving Equation (3) and Equation (4). Specifically, Equation (4) should be

106 solved first for $\frac{\partial \mathbf{X}}{\partial z}$ and $\frac{\partial \mathbf{Y}}{\partial z}$. Then the Equation (3) can be solved in terms of $\mathbf{X}$ and $\mathbf{Y}$. The $z$ represents the spanwise direction, and the

107 coordinate system is shown in the Fig. 2. $\mathbf{X}$ and $\mathbf{Y}$ are the solutions of warping displacements and generalized strain (rotation angles of

108 the cross section and the curvatures of the beam) under unity stress resultant. $n_d$ is the total number of degrees of freedom which equals

109 $3 \times n_n$ where $n_n$ is the number of nodes. The coefficient matrices of these equations contain the information of cross sectional materials

110 and geometry, which are presented in Appendix. A. It should be mentioned here that $\mathbf{X}$ and $\mathbf{Y}$ do not represent the coordinate system

111 here, but the displacement and generalized solution when the resultant $\boldsymbol{\theta}$ equals $\mathbf{I}_6$ (unitary matrix).

$$
\begin{bmatrix}
\mathbf{E}_{(n_d \times n_d)} & \mathbf{R}_{(n_d \times 6)} & \mathbf{D}_{(n_d \times 6)} \\
\mathbf{R}^T_{(6 \times n_d)} & \mathbf{A}_{(6 \times 6)} & \mathbf{0}_{(6 \times 6)} \\
\mathbf{D}^T_{(6 \times n_d)} & \mathbf{0}_{(6 \times 6)} & \mathbf{0}_{(6 \times 6)}
\end{bmatrix}
\begin{bmatrix}
\mathbf{X}_{(n_d \times 6)} \\
\mathbf{Y}_{(6 \times 6)} \\
\boldsymbol{\Lambda_2}_{(6 \times 6)}
\end{bmatrix}
=
$$
$$
\begin{bmatrix}
(\mathbf{C} - \mathbf{C}^T)_{(n_d \times n_d)} & \mathbf{L}_{(n_d \times 6)} \\
\mathbf{L}^T_{(6 \times n_d)} & \mathbf{0}_{(6 \times 6)} \\
\mathbf{0}_{(6 \times n_d)} & \mathbf{0}_{(6 \times 6)}
\end{bmatrix}
\begin{bmatrix}
\frac{\partial \mathbf{X}}{\partial z}_{(n_d \times 6)} \\
\frac{\partial \mathbf{Y}}{\partial z}_{(6 \times 6)}
\end{bmatrix}
+
\begin{bmatrix}
\mathbf{0}_{(n_d \times 6)} \\
\mathbf{I}_{(6 \times 6)} \\
\mathbf{0}_{(6 \times 6)}
\end{bmatrix}
\tag{3}
$$

$$
\begin{bmatrix}
\mathbf{E}_{(n_d \times n_d)} & \mathbf{R}_{(n_d \times 6)} & \mathbf{D}_{(n_d \times 6)} \\
\mathbf{R}^T_{(6 \times n_d)} & \mathbf{A}_{(6 \times 6)} & \mathbf{0}_{(6 \times 6)} \\
\mathbf{D}^T_{(6 \times n_d)} & \mathbf{0}_{(6 \times 6)} & \mathbf{0}_{(6 \times 6)}
\end{bmatrix}
\begin{bmatrix}
\frac{\partial \mathbf{X}}{\partial z}_{(n_d \times 6)} \\
\frac{\partial \mathbf{Y}}{\partial z}_{(6 \times 6)} \\
\boldsymbol{\Lambda_1}_{(6 \times 6)}
\end{bmatrix}
=
\begin{bmatrix}
\mathbf{0}_{(n_d \times 6)} \\
\mathbf{T}_r^T_{(6 \times 6)} \\
\mathbf{0}_{(6 \times 6)}
\end{bmatrix}
\tag{4}
$$

4

112 The $\frac{\partial \mathbf{X}}{\partial z}$, $\frac{\partial \mathbf{Y}}{\partial z}$, $\mathbf{X}$, and $\mathbf{Y}$ can be used to calculate the compliance matrix $\mathbf{F}_s$ and $\mathbf{K}_s$ stiffness matrix for beam model. The $\mathbf{\Lambda_1}$ and

113 $\mathbf{\Lambda_2}$ are Lagrange multipliers associated with warping displacements (constraints on the warping). The other parameters in the matrices,

114 including $\mathbf{E}$, $\mathbf{R}$, and $\mathbf{D}$, has been stated in the Appendix A. The compliance matrix and stiffness matrix in terms of $\frac{\partial \mathbf{X}}{\partial z}$, $\frac{\partial \mathbf{Y}}{\partial z}$, $\mathbf{X}$ and $\mathbf{Y}$ are

115 shown as follows:

$$
\mathbf{F}_s = \left[ \begin{array}{c} \mathbf{X} \\ \frac{\partial \mathbf{X}}{\partial z} \\ \mathbf{Y} \end{array} \right]^T \left[ \begin{array}{ccc} \underset{(n_d \times n_d)}{\mathbf{E}} & \underset{(n_d \times n_d)}{\mathbf{C}} & \underset{(n_d \times 6)}{\mathbf{R}} \\ \underset{(n_d \times n_d)}{\mathbf{C}^T} & \underset{(n_d \times n_d)}{\mathbf{M}} & \underset{(n_d \times 6)}{\mathbf{L}} \\ \underset{(6 \times n_d)}{\mathbf{R}^T} & \underset{(6 \times n_d)}{\mathbf{L}^T} & \underset{(6 \times 6)}{\mathbf{A}} \end{array} \right] \left[ \begin{array}{c} \mathbf{X} \\ \frac{\partial \mathbf{X}}{\partial z} \\ \mathbf{Y} \end{array} \right] \tag{5}
$$

116

$$
\mathbf{K}_s = \mathbf{F}_s^{-1} \tag{6}
$$

117 These equations are the basis of stiffness matrix construction for beam model. The governing equations of the 2D cross-sectional

118 deformation (warping displacements and generalized strains) are Equation (3) and Equation (4). By solving this linear equation system,

119 $\mathbf{X}$ and $\mathbf{Y}$ in the stiffness matrix calculation of Equation (6) can be achieved, which means that the stiffness matrix for the anisotropic

120 beam model can be calculated. In addition, they are also used in Equation (7) to reconstruct the strain through the stress resultant on the

121 cross section. Then the nodal warping displacement $\mathbf{U}$, the generalized strain of beam $\mathbf{\Phi}$, and their first order derivatives can thus be

122 calculated by Equation (2).

123 Since these calculated variables are related to the three-dimensional strain on each cross section element, the nodal strain can be

124 obtained by following Equation (7), which is the basis of stress and strain reconstruction. $\epsilon_n$, $\mathbf{X}_n$, $\mathbf{Y}_n$ and $(\frac{\partial \mathbf{U}}{\partial z})_n$ are nodal value of

125 $\epsilon$, $\mathbf{X}$, $\mathbf{Y}$ and $(\frac{\partial \mathbf{U}}{\partial z})$. $\mathbf{N}_{2d}$ is the shape function for the two-dimensional cross sectional model (four-node element shape function). The

126 formulation about $\mathbf{S}$, $\mathbf{Z}$ and $\mathbf{B}$ in Equation (7) are all presented in the Appendix A.

$$
\underset{(6 \times 1)}{\epsilon_n} = \underset{(6 \times 3)}{\mathbf{S}} \underset{(3 \times 6)}{\mathbf{Z}} \underset{(6 \times 6)}{\mathbf{Y}_n} \underset{(6 \times 1)}{\boldsymbol{\theta}} + \underset{(6 \times 3)}{\mathbf{B}} \underset{(3 \times 3)}{\mathbf{N}_{2d}} \underset{(3 \times 6)}{\mathbf{X}_n} \underset{(6 \times 1)}{\boldsymbol{\theta}} + \underset{(6 \times 3)}{\mathbf{S}} \underset{(3 \times 3)}{\mathbf{N}_{2d}} \underset{(3 \times 6)}{(\frac{\partial \mathbf{U}}{\partial z})_n} \underset{(6 \times 1)}{\boldsymbol{\theta}} \tag{7}
$$

127 *2.2. One-dimensional anisotropic beam model*

128 The finite element formulation of present one-dimensional anisotropic beam model is proposed in the paper [14]. To expand this

129 formulation to a dynamic beam model, Hamilton's principle and an implicit Newmark's method, are used for solving this dynamic

130 equation.

$$
\mathbf{L} = \mathbf{T} - \mathbf{\Pi} + \mathbf{W}_f \tag{8}
$$

131 To construct the dynamic model, the Hamilton's principle (Equation(8)) is used and represented by the Equation (8). $\mathbf{L}$ in this

132 equation is the Lagrangian functional, which is the combination of kinetic energy, potential energy, and the work of external force $\mathbf{W}_f$.

133 In the finite element formulation, the displacement vector $\mathbf{d}$ (6 components) of a beam can be represented by the nodal displacements

134 vector $\mathbf{d}_n$.

$$
\underset{(6 \times 1)}{\mathbf{d}} = \underset{(6 \times 6N_i)}{\mathbf{N}} \underset{(6N_i \times 12)}{\mathbf{N}_\alpha} \underset{(12 \times 1)}{\mathbf{d}_n} \tag{9}
$$

135 In Equation (9), $N_i$ represents the order of the shape function of beam. The details about the parameter matrices can be found in

136 Appendix B. It should be noted here that in order to construct high-order ($N_i > 3$) polynomial shape functions for the two-node element,

137 Kim et al. introduces a new derivation of shape functions by using the total elastic energy minimization method in [14]. The high-order

138 shape function of displacement is required because we need to differentiate the displacement with respect to $z$ to calculate the generalized

5

139 strain of the beam. This makes the formulation of $N_\alpha$ more complicated, which is shown in Appendix B. $N_\alpha$ is implemented in each

140 term of Equation (8). As a result, in the following part, each term in Equation (8) will be represented in form of nodal displacement

141 vector in Equation (9).

142     Firstly, the potential energy (elastic strain energy) can be represented by the following equation.

$$\Pi = \frac{1}{2}\mathbf{d}_n^T \left[ (\mathbf{N}_\alpha)^T \left( \int_{L_e} \mathbf{B}_b(z)^T \mathbf{K}_s \mathbf{B}_b(z)\mathrm{d}z \right) \mathbf{N}_\alpha \right] \mathbf{d}_n$$
$$= \frac{1}{2}\mathbf{d}_n^T \mathbf{K}_e \mathbf{d}_n \tag{10}$$

143 and

$$\mathbf{K}_e = (\mathbf{N}_\alpha)^T \left( \int_{L_e} \mathbf{B}_b(z)^T \mathbf{K}_s \mathbf{B}_b(z)\mathrm{d}z \right) \mathbf{N}_\alpha \tag{11}$$

144     In this equation, $\mathbf{B}_b$ is the first derivative of shape function $\mathbf{N}$. $\mathbf{K}_s$ is the stiffness matrix, which is calculated in Equation (6). The $\mathbf{K}_e$

145 is the local stiffness matrix. $L_e$ here represents the length of the local beam element.

146     The kinetic energy equation is illustrated as follows.

$$\mathbf{T} = \frac{1}{2}\dot{\mathbf{d}}_n^T \left[ (\mathbf{N}_\alpha)^T \left( \int_{L_e} \mathbf{N}(z)^T \mathbf{E}_s \mathbf{N}(z)\mathrm{d}z \right) \mathbf{N}_\alpha \right] \dot{\mathbf{d}}_n$$
$$= \frac{1}{2}\dot{\mathbf{d}}_n^T \mathbf{M}_e \dot{\mathbf{d}}_n \tag{12}$$

147 and

$$\mathbf{M}_e = (\mathbf{N}_\alpha)^T \left( \int_{L_e} \mathbf{N}(z)^T \mathbf{E}_s \mathbf{N}(z)\mathrm{d}z \right) \mathbf{N}_\alpha \tag{13}$$

148     The matrix $\mathbf{E}_s$ can be calculated by the surface integral on the cross section. The coordinate system is presented in Fig. 2. The $\mathbf{M}_e$

149 is the local mass matrix defined in Equation (13) [23].

$$\mathbf{E}_s = \int_A \begin{bmatrix} 1 & 0 & 0 & 0 & 0 & -y \\ 0 & 1 & 0 & 0 & 0 & x \\ 0 & 0 & 1 & y & -x & 0 \\ 0 & 0 & y & y^2 & -xy & 0 \\ 0 & 0 & -x & -xy & x^2 & 0 \\ -y & x & 0 & 0 & 0 & x^2+y^2 \end{bmatrix} dA \tag{14}$$

150     The work of external force is given as follows:

$$\mathbf{W}_f = \mathbf{d}_n^T \int_{L_e} (\mathbf{N}_\alpha)^T \mathbf{N}(z)^T \mathrm{d}z \cdot \mathbf{f} \tag{15}$$

151     In this equation $\mathbf{f}$ is the force on the beam element.

6

152    The above equations from Equation (10) to Equation (15) are in their local forms, which can be assembled into the global form:

$$\mathbf{K}_G D + \mathbf{M}_G \ddot{D} = \mathbf{F}_G \tag{16}$$

153    Here $\mathbf{K}_G$ is the global stiffness matrix. $\mathbf{M}_G$ is the global mass matrix. $\mathbf{F}_G$ is the global external force matrix, and $D$ is the global
154    displacement matrix. Equation (16) is solved by the Newmark's method [24].

155    Firstly, initial values ($^o$) are assigned to the displacement vector and its first and second order time derivatives.

$$D^o = [\mathbf{0}]_{6n_{bn} \times 1} \quad \dot{D}^o = [\mathbf{0}]_{6n_{bn} \times 1} \quad \ddot{D}^o = [\mathbf{0}]_{6n_{bn} \times 1} \tag{17}$$

156    In Equation (17), the $n_b$ is the number of beam nodes.

157    In the first step, the second derivative of displacement can be calculated.

$$\ddot{D}^{n+1} = \mathbf{K}_{cm}^{-1} \mathbf{F}^{n+1,residual} \tag{18}$$

158    $\mathbf{K}_{cm}$ and $\mathbf{F}^{n+1,residual}$ are shown as follows.

$$\mathbf{K}_{cm} = \mathbf{K}_G \beta \Delta t^2 + \mathbf{M}_G \tag{19}$$

$$\mathbf{F}^{n+1,residual} = \mathbf{F}^{n+1} - \mathbf{K}_G \left[ D^n + \Delta t \dot{D}^n + \Delta t^2 \left( \frac{1}{2} - \beta \right) \ddot{D}^n \right] \tag{20}$$

159    In the second step, the displacement and its first derivative at the next time step can be calculated.

$$D^{n+1} = D^n + \Delta t \dot{D}^n + \Delta t^2 \left[ \left( \frac{1}{2} - \beta \right) \ddot{D}^n + \beta \ddot{D}^{n+1} \right] \tag{21}$$

$$\dot{D}^{n+1} = \dot{D}^n + \Delta t \left[ (1 - \gamma) \ddot{D}^n + \gamma \ddot{D}^{n+1} \right] \tag{22}$$

160    Then it returns to the first step. If $2\beta \geq \gamma \geq \frac{1}{2}$, the algorithm is unconditionally stable. If $\gamma = \frac{1}{2}$, the algorithm can achieve 2nd
161    order time accuracy. If $\beta = 0$ and $\gamma = \frac{1}{2}$, the algorithm is the central difference method. If $\beta = \frac{1}{6}$ and $\gamma = \frac{1}{2}$, the algorithm is the linear
162    acceleration method. If $\beta = \frac{1}{4}$ and $\gamma = \frac{1}{2}$, the algorithm is the implicit method. The parameters $\beta$ and $\gamma$ are $\frac{1}{4}$ and $\frac{1}{2}$ respectively to
163    guarantee the unconditional stability of the algorithm.

## 2.3. Aeroelastic modelling

165    In this section, the aeroelastic model will be established by combining the aforementioned beam model (structural model) with an
166    aerodynamic model (BEM model). The aerodynamic force can be determined by the local lift and drag coefficients, $C_l$ and $C_d$, which
167    can be obtained through the look-up table of lift and drag coefficients with respect to the local angle of attack $\alpha$ based on the inflow angle
168    $\phi$, pitch angle $\beta$ and blade twist angle due to the blade torsion $\Delta\beta$:

$$\alpha = \phi - \beta + \Delta\beta \tag{23}$$

169    From the blade element analysis, the local inflow angle $\phi$ can be calculated by using the following equation:

$$\tan\phi = \frac{(U_\infty + U_n')(1 - a) + V_{e-op}}{(\Omega r + U_t')(1 + a') + V_{e-ip}} \tag{24}$$

7

The $V_{e-op}$ and $V_{e-ip}$ are out-of-plane and in-plane velocities induced by the vibration of the blade, which are predicted from the structure model. $U_\infty$ and $\Omega r$ are free stream velocity and rotational velocity respectively. It is assumed that the near wake is stable, the axial and tangential induction factors $a$ and $a'$ are constant, which can be calculated by the blade element momentum (BEM) method. The procedure of BEM can be seen from the Figure 3. The $U_n'$ and $U_t'$ are two components of the fluctuating velocity, which can be obtained from a turbulent wind model to be introduced later.

The aerodynamic forces can be calculated by Equation (25).

$$f_a(\alpha) = L(\alpha)\frac{1}{2}\rho V_{rel}^2 cdr \tag{25}$$

where $L(\alpha)$ is the coefficient matrix from the

$$L(\alpha) = \begin{bmatrix} -\cos\phi & \sin\phi & 0 \\ \sin\phi & \cos\phi & 0 \\ 0 & 0 & 1 \end{bmatrix} \begin{bmatrix} C_d \\ C_l \\ C_m c \end{bmatrix} \tag{26}$$

The $C_m$ and $c$ are aerodynamic moment coefficient and chord respectively. This aerodynamic model can be coupled with the aforementioned structural model (1D anisotropic beam model). The flowchart of the aeroelastic model is shown in Fig. 1.

The $Ris\phi$ model [25] is employed as the dynamic stall model for the lift coefficient, in which the non-dimensional parameter $f$ defined in Equation (32), a measure of the degree of separation, is introduced to correct the aforementioned lift coefficient. The dynamic angle of attack $\alpha_d$ (a function of time $t$) is also introduced which is shown in Equation (27).

$$\alpha_d(t) = \alpha(1 - A_1 - A_2) + c_1(t) + c_2(t) \tag{27}$$

in which $c_1(t)$ and $c_2(t)$ are two variables to describe the delayed lift coefficient. $A_1$ and $A_2$ are two parameters, which are shown in Table 16. The dynamic linear lift is calculated as:

$$C_{l0,d} = C_{l0}(\alpha) + \frac{\pi c\dot{\alpha}}{2V_{rel}} \tag{28}$$

where

$$C_{l0}(\alpha) = \frac{dC_l}{d\alpha}\Big|_{\alpha_0}(\alpha - \alpha_0) \tag{29}$$

in which $\alpha_0$ is the angle of attack under which the lift coefficient is zero. If the separation parameter $f$ is equal to 0 (fully separated condition), the $C_{l0} = 4C_l^{st}$, in which $C_l^{st}$ is from the table checking of static lift coefficients (the superscript "st" means static). The variables can be determined by the following Equation (30). In this equation, $C_{l0}'$ is the retarded lift coefficient. $\alpha_f$ can be calculated by $C_{l0}'$ (see Equation (31)).

$$\begin{bmatrix} \dot{c}_1 \\ \dot{c}_2 \\ \dot{C}_{l0}' \\ \dot{f}_d \end{bmatrix} = \begin{bmatrix} -(\omega_1 + \frac{\dot{V}_{rel}}{V_{rel}}) & 0 & 0 & 0 \\ 0 & -(\omega_2 + \frac{\dot{V}_{rel}}{V_{rel}}) & 0 & 0 \\ 0 & 0 & -\omega_4 & 0 \\ 0 & 0 & 0 & -\omega_3 \end{bmatrix} \begin{bmatrix} c_1 \\ c_2 \\ C_{l0}' \\ f_d \end{bmatrix} + \begin{bmatrix} \omega_1 A_1\alpha \\ \omega_2 A_2\alpha \\ \omega_4 C_{l0,d} \\ \omega_3 f(\alpha_f) \end{bmatrix} \tag{30}$$

$$\alpha_f = C_{l0}'/\frac{dC_l}{d\alpha}\Big|_{\alpha_0} + \alpha_0 \tag{31}$$

8

189 The separation parameter $f$ can be calculated by Equation (32).

$$f(\alpha) = (2\sqrt{\frac{C_{l0}(\alpha)}{C_l^{st}(\alpha)}} - 1)^2 \tag{32}$$

190 The dynamic lift coefficient for aerodynamic model can be calculated by Equation (33).

$$C_{l,d}(t) = f_d(t)C_{l0}(\alpha_d) + (1 - f_d)C_{l1}(\alpha_d) \tag{33}$$

191 In Equation (33), the $C_{l1}$ can be calculated by the following Equation (34).

$$C_{l1}(\alpha_d) = \begin{cases} \dfrac{C_{l0}(\alpha_d)}{2} & f = 1 \\ \dfrac{[C_{l,d}^{st}(\alpha_d) - C_{l0}(\alpha_d)f]}{1 - f} & else \end{cases} \tag{34}$$

192 Two test cases of DU-40 airfoil for the dynamic stall model are carried out with the prescribed change of $\alpha$ shown in equations (35)
193 and (36) below. The parameters for the dynamic stall model are shown in Table 16.

$$\alpha(t) = 5 + 5\sin(12t) \quad (^o) \tag{35}$$

$$\alpha(t) = 20 + 50\sin(12t) \quad (^o) \tag{36}$$

194 The comparison between the static and dynamic (corrected) lift coefficients are compared in Figs. 14 and 15. The lift coefficient for
195 dynamic stall model is slightly different from the static lift coefficient. The dynamic lift coefficients varies along the blue circle, which
196 is the delayed effect. It should be mentioned here that the tower and shaft are not considered in the current aeroelastic model. Due to
197 this, the results presented later only have a qualitative value.

198 *2.4. Fatigue analysis*

199 Three kinds of fatigue analysis methods have been introduced, including the fatigue life models, phenomenological models, and
200 progressive damage models. Among these methods, the progressive damage method is the most promising method because of its
201 capability to deal with multi-axial fatigue analysis. The progressive method can also predict multiple fatigue damage modes, because
202 it is based on the first principles. However, in wind energy industry, the progressive damage model has not been widely adopted in the
203 fatigue life prediction of wind turbine blades. In the authors' views, this is mainly due to its complexity and computational cost. In
204 the GL guidelines for the certification of wind turbines, the fatigue life method is suggested for the fatigue life prediction of composite
205 structures, which consists of the Palmgren-Miner fatigue damage accumulation rule, rainflow counting algorithm, S-N curve, and shifted
206 Goodman diagram. The values of safety factors are also suggested in the GL guidelines. Although it is more efficient, the fatigue life
207 method still has limitations due to its empirical nature. Its accuracy is highly dependent on the precision of the data source, including
208 the S-N curve and Goodman diagram. The data source used in this study is from a recent research paper about the fatigue analysis of the
209 NREL 5MW wind turbine blade [26].

210 The fatigue damage of wind turbine blade material can be calculated by Miner's rule given by Equation (37). The basic assumption
211 of this rule is that the damage can be accumulated linearly and independently.

$$D_p = \sum_i \frac{1}{N(\sigma_{a,i}, \sigma_{m,i})} \tag{37}$$

9

212 In Equation (37), $D_p$ represents the total fatigue damage of the subject material in a certain period. $i$ indicates the stress cycle
213 number. $N$ is the number of cycles to failure in terms of mean stress $\sigma_{m,i}$ and stress amplitude $\sigma_{a,i}$, which can be calculated by the
214 rainflow counting algorithm. By considering S-N curve (stress vs. number of cycles) and constant life diagram (shifted Goodman
215 relationship), the number of cycles to failure $N(\sigma_{a,i}, \sigma_{m,i})$ can be calculated by Equation (39) from the GL certification guideline [22].
216 The life of a wind turbine blade in years can be calculated by using the following Equation (38). $L$ here is the life of the blade material,
217 and $T_p$ is our simulation time.

$$L = \frac{1}{D_p} \frac{T_p}{365 \times 24 \times 3600} \tag{38}$$

$$N(\sigma_{a,i}, \sigma_{m,i}) = \left[ \frac{\sigma_T + |\sigma_C| - 2|\gamma_{M_a}\sigma_{m,i} - \sigma_T + |\sigma_C||}{2\frac{\gamma_{M_b}}{C_{1b}}\sigma_{a,i}} \right]^m \tag{39}$$

218 In Equation (39), $\sigma_T$ and $\sigma_C$ are the ultimate tension and compression strengths (characteristic short-term structure member resis-
219 tance) for tension and compression respectively. $\gamma_{M_a}$ is partial safety factors for material respectively. $m$ is the exponential factor of the
220 S-N curve. $\gamma_{M_b}$ can be calculated by

$$\gamma_{M_b} = \gamma_{M_0} \prod_i C_{ib} \quad (i = 1, 2, 3, 4, 5) \tag{40}$$

221 or

$$\frac{\gamma_{M_b}}{C_{1b}} = \gamma_{M_0} \prod_i C_{ib} \quad (i = 2, 3, 4, 5) \tag{41}$$

222 In the above Equation (40) or (41), $C_{ib}$ represents the safety factor in terms of temperature effect, material fabrication effect etc. The
223 detailed value for each safety factors will be introduced in the following section (see Table 3 and Table 4) in terms of the materials for
224 the NREL 5MW turbine blade. Here $\gamma_{M_0}$ equals 1.35. These safety factors of material are from the GL guidelines for the certification
225 of wind turbines. The flowchart of the fatigue analysis methodology is shown in the Fig. 5.

## 3. Modal and static analysis of the NREL 5MW turbine blade

227 The NREL 5MW wind turbine blade has been extensively used in research related to large wind turbines. Each of its blades is 61.5
228 meters long and weighs 17740 kg. This blade is designed according to the IEC standard, and the information of structural properties can
229 be found in the NREL report [26]. The information about the material properties, layup informations, and blade geometry are obtained
230 from the Sandia report [27]. This wind turbine blade is mainly made of four kinds of composite materials, including triaxial (TRIAX),
231 biaxial (WEB), carbon fibre uniaxial (CUD) and glass fibre (EUD) uniaxial composite materials. The layup of different materials is
232 shown in Fig. 7. The main structure, spar caps, is mainly composed of carbon fibre composite, which endures large normal stress. A
233 glass fibre composite is used to build the trailing edge reinforcement section. A triaxial fibre composite is used to construct the leading
234 edge and trailing edge of the blade. A biaxial fibre composite is the material of shear webs, which can absorb shear forces in the cross
235 section.

236 Here BTC is simply induced by a slight fibre orientation change on the material plies of carbon fibre composite in the spar caps.
237 Although including BTC in caps is complicated and costly from the manufacturing point of view, it is still the most simple and direct
238 way to induce a higher BTC coefficient because the spar caps are the main structure which endure the majority of the bending moment.
239 In fact, the simulation cases presented in this and next sections, more details about BTC in spar caps are discovered and discussed.
240 Here four different orientations ($0^o$, $5^o$, $10^o$ and $15^o$) are researched and compared in this paper. The BTC coefficients of these four
241 different orientations are shown in Fig. 6. The BTC coefficients are calculated by Equation (42). In this equation, $EI$ represents the

10

242 flapwise bending stiffness, $GJ$ indicates the torsional stiffness, and $g$ is the coupling stiffness. The plot of BTC coefficients at different
243 orientations is shown in Fig. 6. Obviously, $15^o$ orientation design has the highest coupling coefficient.

$$\alpha_c = -\frac{g}{\sqrt{EI \times GJ}} \tag{42}$$

244 In this section, modal analysis and static analyses on the NREL 5MW turbine blade are carried out to preliminarily investigate the
245 properties of BTC blade. This investigation shows a big picture about the BTC effect on the dynamic and static response of wind turbine
246 blade. Mathematically, modal analysis is an eigenvalue problem in terms of Equation (16). Both the elastic potential energy and inertia
247 term are considered in the modal analysis part, which are the most important parts for the numerical implementation of the beam model.
248 In addition, the modal analysis is used as a verification case for the present anisotropic beam model. The static analysis can reveal the
249 information about the stress and strain distributions, though inertia effects are neglected in the static analysis. It should be mentioned
250 that the inertial effects and gravitational forces will be carefully considered in the next section of dynamic simulation.

251 For modal analysis, we compute the natural frequencies and discuss the BTC effects on the modes. The computed natural frequencies
252 for the first six modes of an anisotropic beam and the result obtained with 3D ANSYS are compared. The results of 3D ANSYS analysis
253 are from the Resor's paper in 2013 about design of the NREL 5MW turbine blade [27]. From the Table 1, it can be seen that they
254 have a good agreement. Since the mode of the blade is related to the inertia and elastic potential effect, this result verifies the previous
255 formulation and our in-house code for the one-dimensional beam model. For illustration purpose, the first six mode shapes can be seen
256 in Fig. 8.

257 Next, the BTC effects on the natural frequencies of the blades with different spar cap orientations are studied. Specifically, the
258 natrual frequencies for different blades with composites at different orientations on caps are compared in Table 2. It shows that each
259 natural frequency of bending modes for $5^o$, $10^o$, and $15^o$ orientations tends to decrease, which is caused by the reduction of stiffness on
260 longitudinal direction. In contrast, the torsional modes tend to slightly increase. It is also found that edgewise modes are less sensitive to
261 the change of fibre orientation, which means that the edgewise moment is less sensitive to the spar caps orientation change. Because the
262 dominant force in the edgewise direction is gravitational force, the fatigue damage of materials related to the edgewise moments is also
263 less affected by the orientation change.

264 The static analysis is carried out under the condition of rated wind speed (at 11.4 m/s) to study the static response of the wind turbine.
265 The root bending moment of wind turbine blade is always the maximum. For the static stress (not moment) analysis case, it is not
266 always the case. In this case, the aerodynamic force is pre-calculated using the BEM method and the azimuth angle of the blade is $90^o$
267 (clockwise), which means that the blade is directed vertical to the ground. Here only the longitudinal stress and strain are analysed,
268 because they are much larger than the other components and, therefore, more significant for fatigue analysis due to the blade's slender
269 beam structure.

270 The wind turbine blade is made of different composite materials, which have different mechanical properties, including stiffness and
271 strength. Among these materials, carbon fibre composite in the spar caps endures a large proportion of loading, which also means that
272 the stress on the spar caps are much higher than that in the other sections. However, it does not always mean that the spar caps are the
273 most vulnerable part of the blade because different materials have different capabilities of resistance to fatigue damage. For example, the
274 stress on the glass fibre composite (reinforcement section) is much lower than that of carbon fibre (spar caps). But the glass fibre is less
275 resistant to the fatigue damage than carbon fibre. As a result, the fatigue damage of different materials should be analysed separately.
276 This is also the reason why we use BECAS to reconstruct the strain and stress in the cross sections. It should be noted that the stress
277 is not continuously distributed in composite structure along the blade because of the difference in material properties. Fortunately, the
278 strain is continuously distributed. To study the BTC effect, the strain distributions in a wind turbine blade for different orientation cases

11

are firstly provided in Fig. 9a-9d. These figures are produced by reconstructing the strain on different cross sections.

From Fig. 9a, it can be seen that there exists an strain-concentration zone at the transition section of the blade (from round shape to airfoil shape). The materials around the "concentration zone" will have much larger stress than the same materials in other sections. From Fig. 9b-9d for the BTC blades, there exists another "concentration zone" close to the tip around the leading and trailing edges. This is thought to be caused by the BTC effect. The plot of the maximum magnitudes of longitudinal (fibre-direction) stresses of different materials at different cross sections (longitudinal 0 m from root to 45 m from root) are shown in the Fig. 10a-10f. In these figures, the carbon fibre refers to the spar caps, the glass fibre refers to the reinforcement section, the triaxial composite refers to the trailing and leading edge, and the biaxial composite refers to the shear webs. Although the moments are decreasing from the root to the tip, there is a stress peak for different materials in the transition section, which is within the first strain-concentration zone. For shear webs (biaxial composite) and triaxial composite, there is another peak at around the tip, which is within the second strain-concentration zone. To further study the stress and strain distributions of the blade, we randomly choose two cross sections from within these two "concentration zones" as two samples for further analysis. The corresponding longitudinal (fibre-direction) stress and strain distributions are shown in Fig. 11a-11h and Fig. 12a-12h. Fig. 11a-11h are sampled at the 10.25 m section from the root of the blade. From these figures, there are no differences in terms of stress and strain distributions between different BTC blades at the 10.25 m section. In other words, the static responses of this blade section for BTC blades with different fibre orientations are the same. In the aeroelastic simulation and fatigue analysis given in the next section, the peak and valley of stress values on this section will be minimized by the BTC effect, and the fatigue mitigation effect will be shown. Fig. 12a-12h are sampled at the 30m section, where the orientation of carbon fibre are induced. Two important things can be observed in these figures. The maximum stress is slightly reduced by the orientations induced in the spar caps. Since the maximum stress exists in the spar caps, so the load of carbon fibre will be alleviated. On the other hand, the loading for other materials is increasing, because the strain value is increasing, which can be seen in these figures. In the authors' view, the shear webs that are most close to the spar caps will endure an increase in stress.

## 4. Preliminary aeroelastic simulation and fatigue analysis of the NREL 5MW wind turbine

In this section, preliminary aeroelastic simulation (dynamic simulation without dynamic stall model) and fatigue analysis (without considering wide range of wind speed) is carried out for the NREL 5MW wind turbine. The rotational speed is 12.1 rpm, the wind speed is 11.4 m/s and the turbulence intensity is 10%. It is assumed that the wind speed is uniformly distributed in all wind directions. The fluctuating wind speed is simulated by the Sandia method [28]. In this method, the fluctuating wind speed is assumed to be coloured noise, whose spectrum (Kaimal spectrum) is shown in Equation (43).

$$\frac{fS_k(f)}{\sigma_k^2} = \frac{4fL_k/V_{hub}}{\left(1 + 6fL_k/V_{hub}\right)^{\frac{5}{3}}} \tag{43}$$

where $f$ is the frequency in Hz, $k$ is the index referring to the velocity component direction (1 = longitudinal, 2 = lateral, 3 = upward), $S_k(f)$ is the single-sided velocity component spectrum, $\sigma_k$ is the velocity standard deviation, $L_k$ is the velocity component integral scale parameter, and $V_{hub}$ is the wind velocity at the hub height. Instead of using a white noise, the transformation matrix can be obtained from the above spectrum, by which the matrix is used to generate the simulated wind speed in frequency domain. Lastly the wind speed can be recovered by employing the inverse Fourier transform.

The methodology of aeroelastic simulation and fatigue analysis has already been presented in previous sections. For fatigue analysis, the safety factors, thickness and strength of different materials of NREL 5MW turbine blade can be seen in Tables 3 and 4. In Table 3, the $\gamma_{M_a}$ is the partial safety factor for the material. $C_{ib}$ represents the safety factor in terms of temperature effect, material fabrication effect, etc. The fatigue properties of $0^o$ UD composite will be different from that of other UD composites with offset angles. To apply

the properties of $0^o$ UD, material coordinate system is employed for the UD composites with offset angles, which is explained in the BECAS manual (2015, page 60-61). The longitudinal stress can be transformed to the material coordinate system (along the fibre) by multiplying the rotation matrix.

### 4.1. Fatigue analysis of single wind turbine under normal wind condition

This section studies the wake effect on the loading, tip displacements, and the fatigue damage of a single wind turbine with different orientations of carbon fibre will be compared under the normal wind condition (turbulence intensity of 0.1). The fluctuating wind speed is shown in Fig. 13. The fluctuating root bending moments of each blade are illustrated in the Fig. 16. It can be seen that the minimization of the peaks and valleys of fluctuating flapwise bending moments is achieved by the BTC effect. With an increase in orientation angle, the mitigation effect is more obvious. For the edgewise bending moment, the mitigation effect is not observed, because the edgewise bending moment is dominated by the gravity force instead of the aerodynamic force. For the tip displacements, both the flapwise and edgewise tip displacements of BTC blades are shifted upward, which can be seen in the Fig. 17. In the figure of edgewise displacement, the amplitudes of vibrations are 1.5476m, 1.5975m, 1.6795m, and 1.7648m for the 0, 5, 10, and 15 offset angles respectively. In other words, there exists an increase of the amplitudes with the increase of offset angles. Compared with blades without the BTC effect, the shifted values of the flapwise and edgewise displacements for the $15^o$ BTC blade are 2m and 0.2m respectively. This extra tip displacement will affect the designed gap between the blade and tower. Fig. 18 shows the minimum fatigue life of different materials on different cross sections. There is a lowest point of fatigue life for different materials. The values of the lowest points are shown in the Fig. 19. If we recall the "strain-concentration" zone in the previous section, the lowest point is located at this zone (10m from the root). This fatigue damage is caused by the large strain (or stress) value for different materials. From our calculations, it should be noted that the longevity of carbon fibre composite in spar caps, which is the main structure, has increased with the increase in orientation angle due to the BTC effect. For the section around the tip, the fatigue mitigation effect is obvious for spar caps. In fact, the lowest value of fatigue life in spar caps increases from 337 years to 404 years for the $15^o$ case. It should be noticed that this fatigue mitigation effect is due to the aforementioned peak-valley minimization in terms of bending moments. The fatigue life of other materials, including EUD, TRIAX, does not change too much.

### 4.2. Fatigue analysis of multiple wind turbines under wake condition

In this section, wake effect on the wind turbine blade is considered, which is also an important factor for fatigue load increase. This wake condition is also referred to as the IEC61400-1 standard for wind turbines. The effective turbulence intensity in the wake region can be calculated by using the following equations. It is assumed that the wind speed is uniformly distributed in all wind directions.

$$I_{eff} = \frac{\hat{\sigma}_{eff}}{V_{hub}} = \frac{1}{V_{hub}}[(1 - Np_w)\hat{\sigma}^m + p_w \sum_{i=1}^{N} \hat{\sigma}_T^m(d_i)]^{\frac{1}{m}} \tag{44}$$

$$\hat{\sigma}_T = \sqrt{\frac{0.9V_{hub}^2}{1.5 + 0.3d_i\sqrt{V_{hub}}} + \hat{\sigma}^2} \tag{45}$$

In Equation (44), $I_{eff}$ is the effective turbulence intensity under the wake condition. $\hat{\sigma}_{eff}$ is the standard turbulence deviation under wake condition. $V_{hub}$ is the wind speed at the hub height (11.4 m/s in this case). $N$ is the number of neighbouring turbines. $p_w$ is a constant (0.06 for evenly distributed wind speed). $\hat{\sigma}_T$ is the added turbulence standard deviation. $m$ is the coefficients for the S-N curve. $\hat{\sigma}$ is the ambient turbulence standard deviation.

Two different layouts are analysed, including three wind turbines in a line, and nine wind turbines in three arrays. The longitudinal distance is 5D (D is the diameter of the wind turbine rotor). The lateral distance is 3D. From Fig. 20, it can be seen that the turbulence

intensity for three arrays of wind turbine is much higher than that of the three turbines in a line. In this figure, the percentage number beside the circle represents the turbulence intensity. In Fig. 21, each bar represents the aforementioned "lowest point" for different materials at different cross sections, which are also the lowest fatigue lives of different materials at different sections. As a result, Fig. 21 shows the fatigue life of different materials under different wake conditions. It should be noted that the wake mitigation effect for spar caps is obvious for different cases. Noticeably, the percentage of load alleviation effect of BTC is from 20% to 25%. There exists a large decrease of life for both CUD (spar caps) and BIAX (shear webs) under the wake condition. The high turbulence intensity in the wake region will induce large stress fluctuations, which will directly affect the fatigue life of CUD that endures large loading.

## 5. Fatigue analysis with dynamic stall model and under a wide range of wind speed

In this section, the fatigue life of materials of wind turbine blade will be calculated under a wide range of wind speed conditions (design load cases (DLC) power production condition in IEC 61400-1). The turbulence intensity for different wind conditions is calculated based on the normal turbulence model (NTM), and the dynamic stall effect is also considered in this case.

### 5.1. Dynamic stall effect

The simulated dynamic loading of the numerical model with and without dynamic stall model are compared in Fig. 22. From this figure, it can be seen that the fluctuating patterns in the initial period are obviously different during the period from 0 s to 10 s. In this period, the wind turbine blade is loaded with aerodynamic force. The fluctuation part (with the mean value subtracted) of out-of-plane moments are further compared with each other, and this is shown in Fig. 23. The power spectrum for the fluctuation parts of the simulated loading with and without dynamic stall model is further compared in Fig. 24, from which it can be seen that the two fluctuations share the same spectrum for the low frequency (below 1 Hz).

### 5.2. Fatigue life analysis for single wind turbine

In the previous sections, the fatigue analysis of the blade is performed based only on the simulations at one wind speed (11.4 m/s). Moreover, the analysis is performed at a turbulence intensity of 10 %. This is of course not representative of the conditions encountered by a wind turbine which operates in a wide range of wind velocities (3-25 m/s). In order to obtain the realistic values of the fatigue damage, simulations are performed over the whole range of operational conditions. The weights of the different wind conditions are introduced through a representative Weibull distribution. In addition, the turbulence intensity are also calculated according to IEC 61400-1. In other words, a realistic fatigue spectrum will be composed in order to deal with the realistic lifetime results in this section. The wind turbine is analysed under the condition of wind class IB and power production (design load case 1.2 with normal turbulence model) in IEC 61400-1. For wind class IB, the reference turbulence intensity is 0.14 according to IEC 61400-1. The standard deviation of velocity for different wind speed (at hub height) can be calculated by Equation (46).

$$\sigma_1 = I_{ref}(0.75V_{hub} + 5.6) \tag{46}$$

The Equation (47) is the function of Weibull distribution, which is the probability density function of wind speed in wind farm. The plot of Weibull distribution is shown in Fig. 25 ($k = 2.2, c = 11.28$).

$$f(V) = (\frac{k}{c})(\frac{V}{c})^{k-1}e^{-(\frac{V}{c})^k} \tag{47}$$

The simulated wind speed and loading (out-of-plane moments) for different wind speeds are shown in Figs. 26 and 27. The control strategy of wind turbine can be divided into two stages. In the first stage, from 0 - 11.4 m/s (rated wind speed), the rotational speed of

14

rotor is the control variable to optimize the power production (optimum tip speed ratio (TSR)), and the pitch angle is $0^o$. In the stage 2, from 11.4 - 25.0 m/s, the rotational speed is fixed (at 12.1 rpm), and the pitch angle becomes the control variable. The data for these parameters is shown in Table 5 along with the turbulence intensity.

The fatigue lives for different materials under different wind conditions are calculated based on the fatigue damage of the 10.25 m section, which are shown in Table 6. From this table, it can be seen that the lives for different wind speed conditions are very different. The life at around rated wind speed (9 - 13 m/s) is the lowest one for all the materials. The total calculated lives for different materials are shown in Table 7. It should be mentioned here that the calculated life of main structure, carbon fibre composite on the spar caps (CUD), is very close to the design life, 20 years. The biaxial composite in the shear webs (WEB) has the shortest life, 2.62 years. In next section, the fatigue life of different materials under wake conditions will be presented to show fatigue-induced fatigue damage.

*5.3. Fatigue life analysis for wind turbine under wake conditions and compact layout*

For the fatigue life of turbine 8, WT8, (see Fig. 20, 9 wind turbines in array), the wake effects will be considered, and the turbulence intensity under wake conditions will be calculated by Equation (46). The parameters are shown in Table 8. The simulated wind speed and root out-of-plane bending moments are shown in Figs. 28 and 29 respectively. The calculated fatigue lives for different materials under different wind conditions are shown in Table 9. By comparing Table 9 with Table 6 (no wake), the fatigue lives of different materials all decrease under wake conditions. The calculated fatigue life for the main structure (CUD) is much lower than that of 26.0187 years in Table 7 under no wake conditions. The wake-induced fatigue is obvious. This is also because, in authors' view, the layout is too compact. The lateral distance is 3D, and longitudinal distance is 5D. Normally, the lateral and longitudinal distances are at least 5D and 7D respectively.

*5.4. Fatigue life analysis for wind turbine under wake conditions and normal layout*

In this section, the fatigue life for wind turbine (WT8) under wake conditions and normal wind farm layout (9 wind turbines in array, 5D for lateral distance and 7D for longitudinal distance) is calculated. The parameters for different wind speed conditions are shown in Table 11. The simulated wind speeds and out-of-plane root bending moments are illustrated in Figs. 30 and 31. The fatigue analysis results are shown in Tables 12 and 13. When compared these two tables with Table 6 (no wake), it can be seen that the wake effect is still very significant to the fatigue life of wind turbine blade. The fatigue life of spar caps (main structure of CUD) drops from 26.0187 years in Table 7 to 6.9084 years in Table 13. Although some less dominant factors are not considered in this case, i.e. non-uniform wind directions, it still can be concluded that the wake-induced fatigue has an large impact on the fatigue life of wind turbine blade. Compared the results in Table 13 with that in Table 10 (compact layout), the fatigue life increases from 1.7388 years to 6.9084 years. It can be concluded that the layout of wind turbine also has an impact on the fatigue damage of wind turbine blades. Next the performance of BTC blade for WT8 with $15^o$ fibre orientation on the carbon fibre composite in the spar caps in the previous section is studied. The fatigue lives of different materials in BTC wind turbine blade are shown in Tables 14 and 15. The fatigue damage is alleviated by introducing the bend-twist coupling effect. Comparing the fatigue life of carbon fibre composite in BTC blade with that of normal wind turbine blade under wake condition, it can be found that the total fatigue life of CUD increases from 6.9084 years in Table 13 to 6.9532 years in Table 15. But the fatigue load alleviation effect is still obvious in some wind speed range, e.g. 11-15 m/s (comparing Tables 12 and 14).

## 6. Conclusions

In this study, the aeroelastic model is established by combining the BEM method with the anisotropic beam model; the latter is based on a two-dimensional sectional analysis model. In contrast with most studies in this realm, stress life method is employed in this study to analyse the fatigue life of different composite materials on different sections in a wind turbine blade under different wake conditions.

417 The in-house Matlab code of structural model is verified in the present study by comparing its predicted natural frequencies with ANSYS
418 results. Both of the static and modal analysis show that the BTC design will also change the structural properties of the blade, such as
419 natural frequencies, static stress, and strain contours. By using aeroelastic simulation and fatigue analysis method, the fatigue life of
420 single turbine under normal wind condition and multiple wind turbines under wake conditions is analysed. The conclusions are given as
421 follows:

422 (1) From the modal and static analysis of BTC wind turbine blade with different orientations, it is found that BTC design will
423 change the structural properties of the blade in terms of modal frequencies and static response. Specifically, for modal frequencies, the
424 frequencies of the flapwise modes have an obvious decline because of the BTC. The frequencies of the edgewise modes is less sensitive to
425 the BTC. The frequencies of the torsional modes have a slightly increase. For the static response, the static response of sections without
426 BTC does not change. In the sections with BTC, the stress on the spar caps is slightly alleviated, but the strain of other materials has an
427 increase, and two strain concentration zones are found in the static analysis of BTC blade. The first strain concentration zone (10.25 m
428 from root) is also found in the blade without BTC. The second concentration zone (30-50 m from root) is due to the BTC design.

429 (2) From the fatigue analysis of single wind turbine under normal wind conditions, it is found that the "peak and valley" minimization
430 effect is induced by using BTC. In the analysis of fatigue life of different materials on different cross sections, it can be seen that there
431 exists a "lowest point" of fatigue life for different materials at around the first strain concentration zone (10.25 m from root).

432 (3) From the fatigue analysis of multiple wind turbines under wake conditions. it is found that the predicted fatigue life (26.0187
433 years) of the main structure is very close to the design life (20 years). From the fatigue analysis for wind turbine blade in wake conditions,
434 it is found that the wake-induced fatigue has a significant impact on the fatigue life of wind turbine blades (fatigue life drops from 26.0187
435 years to 1.7388 years under compact layout), and wind farm layout can affect the wake-induced fatigue damage (increase from 1.7388
436 years (compact layout) to 6.9084 years (normal layout)). Furthermore, it is also found that the bend-twist coupling wind turbine blade
437 can alleviate the fatigue load under wake condition.

### 7. Acknowledgement

### Appendix A   Two-dimensional cross-sectional model (BECAS)

443 The elements in parameter matrices for 2D sectional model (from Equation (3) to Equation (4)) are listed in this appendix. All of
444 these information is summarized from the BECAS tutorial [21]. Most of the parameters are about surface integral of blade section.

$$\mathbf{A}_{(6 \times 6)} = \sum_{e=1}^{n_e} \int_A \mathbf{Z}_e^T \mathbf{S}_e^T \mathbf{Q}_e \mathbf{S}_e \mathbf{Z}_e dA \tag{A.1}$$

$$\mathbf{R}_{(n_d \times 6)} = \sum_{e=1}^{n_e} \int_A \mathbf{B}_e^T \mathbf{Q}_e \mathbf{S}_e \mathbf{Z}_e dA \tag{A.2}$$

$$\mathbf{E}_{(n_d \times n_d)} = \sum_{e=1}^{n_e} \int_A \mathbf{B}_e^T \mathbf{Q}_e \mathbf{B}_e dA \tag{A.3}$$

$$\mathbf{C}_{(n_d \times n_d)} = \sum_{e=1}^{n_e} \int_A \mathbf{B}_e^T \mathbf{Q}_e \mathbf{S}_e \mathbf{N}_{2d,e} dA \tag{A.4}$$

16

$$\mathop{\mathbf{L}}_{(6 \times n_d)} = \sum_{e=1}^{n_e} \int_A \mathbf{Z}_e^T \mathbf{S}_e^T \mathbf{Q}_e \mathbf{S}_e \mathbf{N}_{2d,e} dA \tag{A.5}$$

$$\mathop{\mathbf{M}}_{(n_d \times n_d)} = \sum_{e=1}^{n_e} \int_A \mathbf{N}_{2d,e}^T \mathbf{S}_e^T \mathbf{Q}_e \mathbf{S}_e \mathbf{N}_{2d,e} dA \tag{A.6}$$

$$\mathop{\mathbf{D}}_{(n_d \times 6)} = \begin{bmatrix} \mathbf{I}_3 & \cdots & \mathbf{I}_3 \\ \mathbf{n}_1 & \cdots & \mathbf{n}_{n_n} \end{bmatrix}^T \tag{A.7}$$

In Equation (A.7), $\mathbf{n}$ has the same form of the $\mathbf{n}_e$ in Equation (A.10), and $\mathbf{I}_3$ is a unitary matrix. In those equations, $\mathbf{N}_{2d,e}$ is the two-dimensional shape function for a finite element on the cross section of the blade, which is four-node element in this study. $\mathbf{Q}_e$ is the elementary material constitutive matrix in Hooke's law, in which $\boldsymbol{\sigma}_e = \mathbf{Q}_e \boldsymbol{\epsilon}_e$ ($\boldsymbol{\sigma}_e$ is the elementary stress and $\boldsymbol{\epsilon}_e$ is the elementary strain).

$$\mathbf{B}_e = \begin{bmatrix} \frac{\partial}{\partial x} & 0 & 0 \\ 0 & \frac{\partial}{\partial y} & 0 \\ \frac{\partial}{\partial y} & \frac{\partial}{\partial x} & 0 \\ 0 & 0 & \frac{\partial}{\partial x} \\ 0 & 0 & \frac{\partial}{\partial y} \\ 0 & 0 & 0 \end{bmatrix} \tag{A.8}$$

$$\mathop{\mathbf{Z}_e}_{(3 \times 6)} = \begin{bmatrix} \mathbf{I}_3 & \mathbf{n}_e \end{bmatrix} \tag{A.9}$$

$$\mathbf{n}_e = \begin{bmatrix} 0 & 0 & y \\ 0 & 0 & -x \\ -y & x & 0 \end{bmatrix} \tag{A.10}$$

$$\mathbf{S}_e = \begin{bmatrix} 0 & 0 & 0 \\ 0 & 0 & 0 \\ 0 & 0 & 0 \\ 1 & 0 & 0 \\ 0 & 1 & 0 \\ 0 & 0 & 1 \end{bmatrix} \tag{A.11}$$

$$\mathbf{T}_r = \begin{bmatrix} 0 & 0 & 0 & 0 & -1 & 0 \\ 0 & 0 & 0 & 0 & 1 & 0 \\ 0 & 0 & 0 & 0 & 0 & 0 \\ 0 & 0 & 0 & 0 & 0 & 0 \\ 0 & 0 & 0 & 0 & 0 & 0 \\ 0 & 0 & 0 & 0 & 0 & 0 \end{bmatrix} \tag{A.12}$$

17

<sub>459</sub> **Appendix B   One-dimensional beam model**

<sub>460</sub>     This appendix is about the parameters of one dimensional anisotropic beam model. The derivation of the model can be found in [14].

<sub>461</sub> To begin with, the shape function is given as follows:

$$\mathop{\mathbf{N}}_{(6\times24)} = \begin{bmatrix} \mathop{\mathbf{I}}_{(6\times6)} & \mathop{z\mathbf{I}}_{(6\times6)} & \mathop{(z)^2\mathbf{I}}_{(6\times6)} & \mathop{(z)^3\mathbf{I}}_{(6\times6)} \end{bmatrix} \tag{B.1}$$

<sub>462</sub>     Where $z$ in Equation (B.1) is defined in Figure 1. The following equations are used to deal with $\mathbf{N}_\alpha$ from Equation (9). $z_1$ and $z_2$ are

<sub>463</sub> the $z$ positions of two nodes of one beam element.

$$\mathop{\mathbf{N}_d}_{(24\times24)} = \begin{bmatrix} \mathop{\mathbf{N}(z_1)}_{(12\times24)} \\ \mathop{\mathbf{N}(z_2)}_{(12\times24)} \end{bmatrix} = \begin{bmatrix} \mathop{\mathbf{N}_1}_{(24\times12)} & \mathop{\mathbf{N}_2}_{(24\times12)} \end{bmatrix} \tag{B.2}$$

<sub>464</sub>

$$\mathop{\mathbf{A}_{\alpha1}}_{(6\times24)} = \begin{bmatrix} \mathop{\mathbf{I}}_{(12\times12)} \\ \mathop{\mathbf{0}}_{(12\times12)} \end{bmatrix} \tag{B.3}$$

<sub>465</sub>

$$\mathop{\mathbf{A}_{\alpha2}}_{(6\times24)} = \begin{bmatrix} \mathop{\mathbf{0}}_{(12\times12)} \\ \mathop{\mathbf{I}}_{(12\times12)} \end{bmatrix} \tag{B.4}$$

<sub>466</sub>

$$\mathbf{Y}_1 = \mathbf{A}_{\alpha1}\mathbf{N}_1^{-1} \tag{B.5}$$

<sub>467</sub>

$$\mathbf{Y}_2 = \mathbf{A}_{\alpha2} - \mathbf{A}_{\alpha1}\mathbf{N}_1^{-1}\mathbf{N}_2 \tag{B.6}$$

<sub>468</sub>

$$\mathbf{B}_s = \mathbf{T}_r\mathbf{N}(z') + \mathbf{I}_6\mathbf{N}'(z) \tag{B.7}$$

<sub>469</sub>

$$\mathbf{D}_s = \int_{z_1}^{z_2} \mathbf{B}_s^T\mathbf{K}_s\mathbf{B}_s dz \tag{B.8}$$

<sub>470</sub>

$$\mathbf{P} = \mathbf{Y}_2^T\mathbf{D}_s\mathbf{Y}_1 \tag{B.9}$$

<sub>471</sub>

$$\mathbf{Q} = -\mathbf{Y}_2^T\mathbf{D}_s\mathbf{Y}_2 \tag{B.10}$$

<sub>472</sub> Lastly, the formula of $\mathbf{N}_\alpha$ is as follows:

$$\mathbf{N}_\alpha = \mathbf{Y}_1 + \mathbf{Y}_2\mathbf{Q}^{-1}\mathbf{P} \tag{B.11}$$

<sub>473</sub>

## 8. References

[1] J. Montesano, H. Chu, C. V. Singh, Development of a physics-based multi-scale progressive damage model for assessing the durability of wind turbine blades, Composite Structures 141 (2016) 50–62.

[2] C. L. Bottasso, A. Croce, F. Gualdoni, P. Montinari, Load mitigation for wind turbines by a passive aeroelastic device, Journal of Wind Engineering and Industrial Aerodynamics 148 (2016) 57–69.

[3] T. K. Ã. Barlas, G. A. M. V. Kuik, Progress in Aerospace Sciences Review of state of the art in smart rotor control research for wind turbines, Progress in Aerospace Sciences 46 (1) (2010) 1–27.

[4] K. Hayat, S. K. Ha, Load mitigation of wind turbine blade by aeroelastic tailoring via unbalanced laminates composites, Composite Structures 128 (2015) 122–133.

[5] F. L. Ponta, A. D. Otero, A. Rajan, L. I. Lago, Energy for Sustainable Development The adaptive-blade concept in wind-power applications, Energy for Sustainable Development 22 (2014) 3–12.

[6] D. W. Lobitz, P. S. Veers, Load mitigation with bending/twist-coupled blades on rotors using modern control strategies, Wind Energy 6 (2) (2003) 105–117.

[7] A. R. Stäblein, M. H. Hansen, G. Pirrung, Fundamental aeroelastic properties of a bendtwist coupled blade section, Journal of Fluids and Structures 68 (October 2016) (2017) 72–89.

[8] A. Dal Monte, S. De Betta, M. Raciti Castelli, E. Benini, Proposal for a coupled aerodynamic structural wind turbine blade optimization, Composite Structures 159 (2017) 144–156.

[9] Z. Chen, K. Stol, B. Mace, Wind turbine blade optimisation with individual pitch and trailing edge flap control, Renewable Energy 103 (2017) 750–765.

[10] M. O. L. Hansen, J. N. Sørensen, S. Voutsinas, N. Sørensen, H. A. Madsen, State of the art in wind turbine aerodynamics and aeroelasticity, Progress in Aerospace Sciences 42 (2006) 285–330.

[11] J. A. Epaarachchi, P. D. Clausen, The development of a fatigue loading spectrum for small wind turbine blades, Journal of Wind Engineering and Industrial Aerodynamics 94 (2006) 207–223.

[12] D. H. Hodges, C. E. S. Cesnik, B. Popescu, B. H. Textron, Assessment of beam modeling methods for rotor blade applications, Material and Computer Modelling 33 (2001) 1099–1112.

[13] V. Giavotto, M. Borri, P. Mantegazza, G. Ghiringhelli, V. Carmaschi, G. Maffioli, F. Mussi, Anisotropic beam theory and applications, Computers & Structures 16 (1-4) (1983) 403–413.

[14] T. Kim, A. M. Hansen, K. Branner, Development of an anisotropic beam finite element for composite wind turbine blades in multibody system, Renewable Energy 59 (2013) 172–183.

[15] P. S. Veers, T. D. Ashwill, H. J. Sutherland, D. L. Laird, D. W. Lobitz, D. A. Griffin, J. F. Mandell, W. D. Msial, K. Jackson, M. Zuteck, A. Miravete, S. W. Tsai, J. L. Richmond, Trends in the design, manufacture and evaluation of wind turbine blades, Wind Energy 6 (3) (2003) 245–259.

[16] K. Thomsen, S. Poul, Fatigue loads for wind turbines operating in wakes, Journal of Wind Engineering 80 (1999) 121–136.

[17] S. Lee, M. Churchfield, P. Moriarty, J. Jonkman, J. Michalakes, Atmospheric and Wake Turbulence Impacts on Wind Turbine Fatigue Loading, NREL Report (December 2011).

[18] A. Rezaeiha, R. Pereira, M. Kotsonis, Fluctuations of angle of attack and lift coef fi cient and the resultant fatigue loads for a large Horizontal Axis Wind turbine, Renewable Energy 114 (2017) 904–916.

[19] A. P. Vassilopoulos, Introduction to the fatigue life prediction of composite materials and structures: past, present and future prospects, Woodhead Publishing (2010) 1–10.

[20] L. Nijssen, Fatigue Life Prediction and Strength Degradation of Wind Turbine Rotor Blade, Ph. D. Thesis (2006) 8–11.

[21] J. P. Blasques, M. Stolpe, Multi-material topology optimization of laminated composite beam cross sections, Composite Structures 94 (11) (2012) 3278–3289.

[22] GL, Guideline for the Certification of Wind Turbines, Lloyd Rules and Guidelines, IVIndustrial Services (2010) 155 – 164(pdf).

[23] P. Blasques, R. Bitsche, V. Fedorov, M. Eder, Applications of the BEam Cross Section Analysis Software ( BECAS ) (2013) 1–4.

[24] N. M. Newmark, A method of computation for structural dynamics, Journal of Engineering Mechanics 85 ((EM3)) (1959) 67–94.

[25] J. W. Larsen, S. R. K. Nielsen, S. Krenk., Dynamic stall model for wind turbine airfoils., Journal of fluids and structures. 23(2007) (2007.) 959–982.

[26] J. Jonkman, S. Butterfield, W. Musial, G. Scott, Definition of a 5-MW reference wind turbine for offshore system development, Contract (February) (2009) 1–75.

[27] B. R. Resor, Definition of a 5MW/61.5m Wind Turbine Blade Reference Model (Sandia Report) (2013) 50.

[28] P. Veers, Three Dimensional Wind Simulation (Sandia Report) (1988) 40.
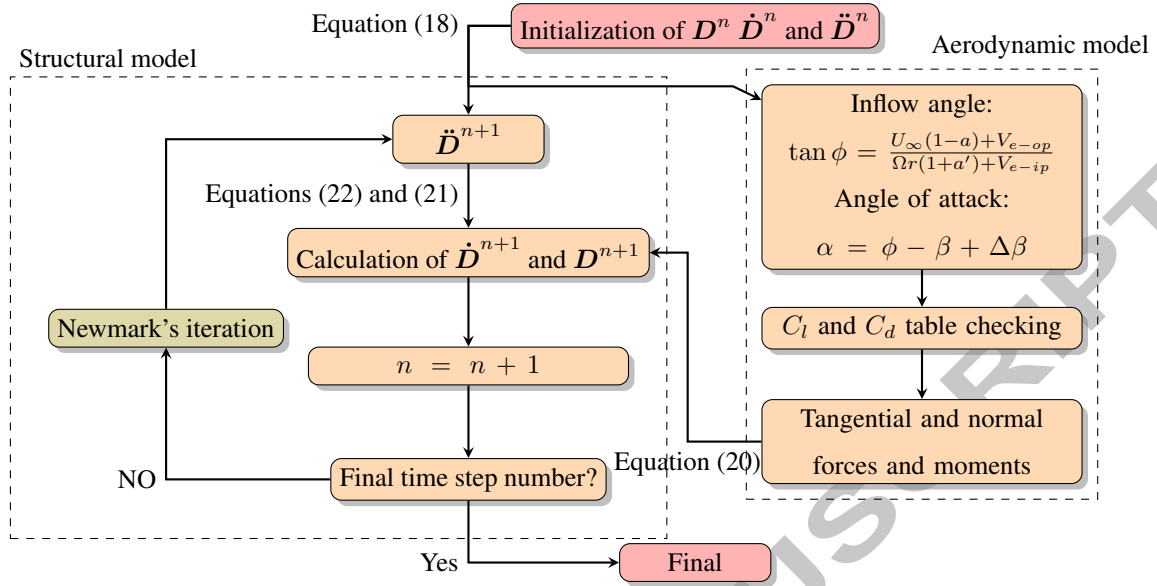
9. Figures



Figure 1: Flowchart of the aeroelastic model.

Structural model

Equation (18)

Initialization of $D^n$ $\dot{D}^n$ and $\ddot{D}^n$

Aerodynamic model

$\ddot{D}^{n+1}$

Equations (22) and (21)

Calculation of $\dot{D}^{n+1}$ and $D^{n+1}$

Newmark's iteration

$n = n + 1$

NO

Final time step number?

Equation (20)

Yes

Final

Inflow angle:

$$\tan\phi = \frac{U_\infty(1-a)+V_{e-op}}{\Omega r(1+a')+V_{e-ip}}$$

Angle of attack:

$$\alpha = \phi - \beta + \Delta\beta$$

$C_l$ and $C_d$ table checking

Tangential and normal forces and moments
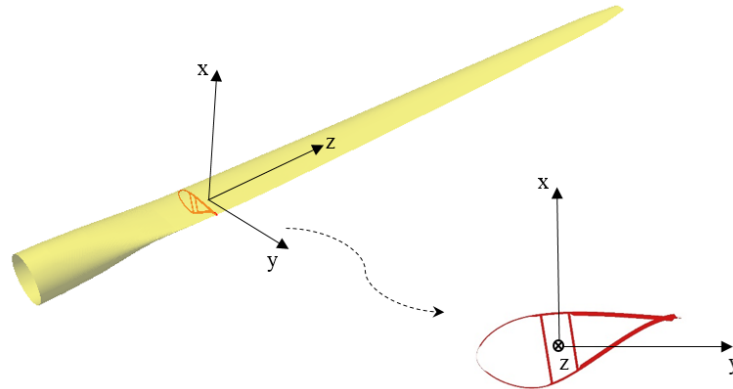


Figure 2: Coordinate system of a wind turbine blade.
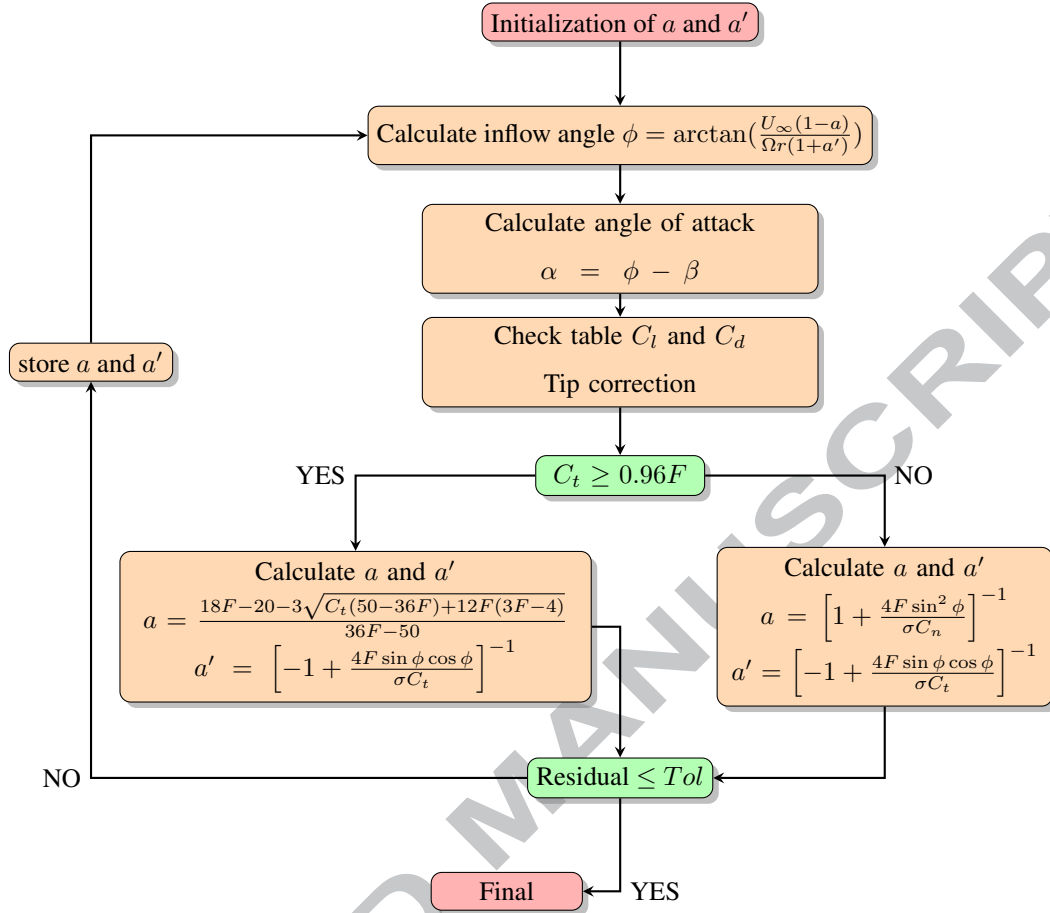
Figure 3: Flowchart of blade element momentum method.
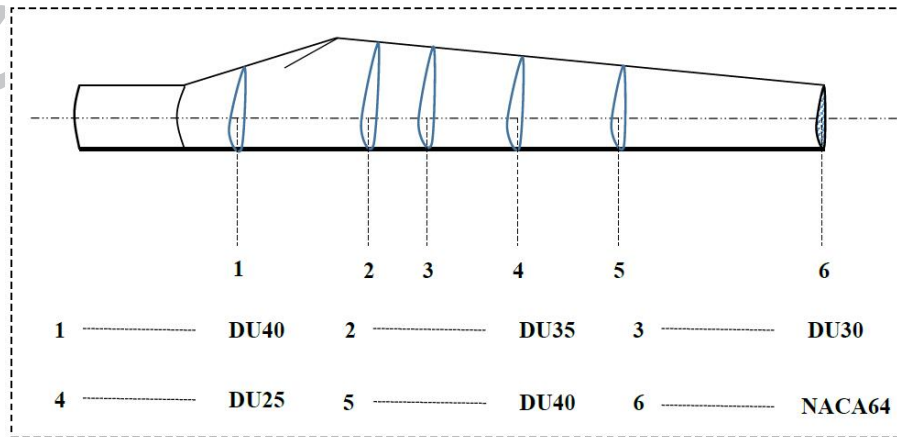


Figure 4: The location of 6 different airfoils in the NREL 5MW turbine blade.

Stiffness matrix $\mathbf{K}_s$ — 2D sectional analysis, BECAS

Aeroelastic model

Anisotropic beam model — coupling — Aerodynamic model

Newmark's iteration

Stress recovery

Displacement history of beam → Sectional force and moment

Strain and stress time history ← Equation (7)

Fatigue analysis

Rainflow counting algorithm — Shifted Goodman diagram / S-N curve — Fatigue life estimation
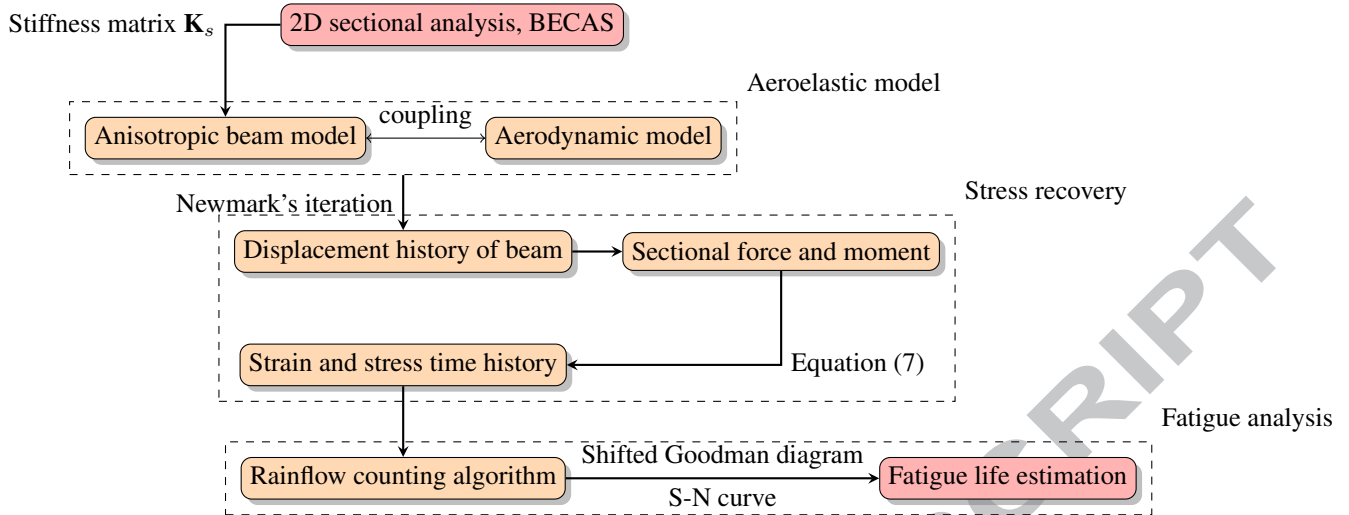
Figure 5: Flowchart of the structure of methodology.
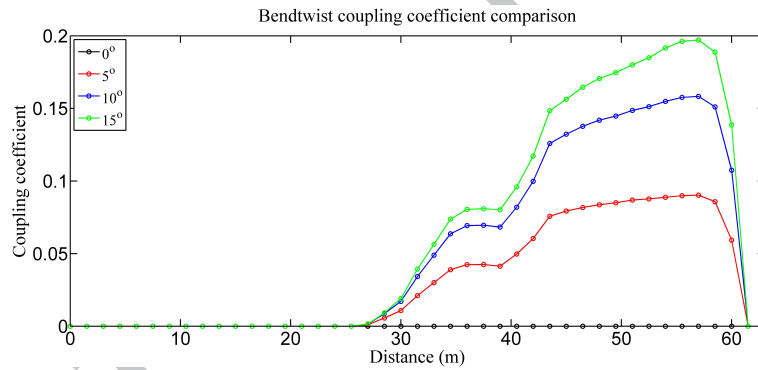


Figure 6: BTC coefficients for different orientations.
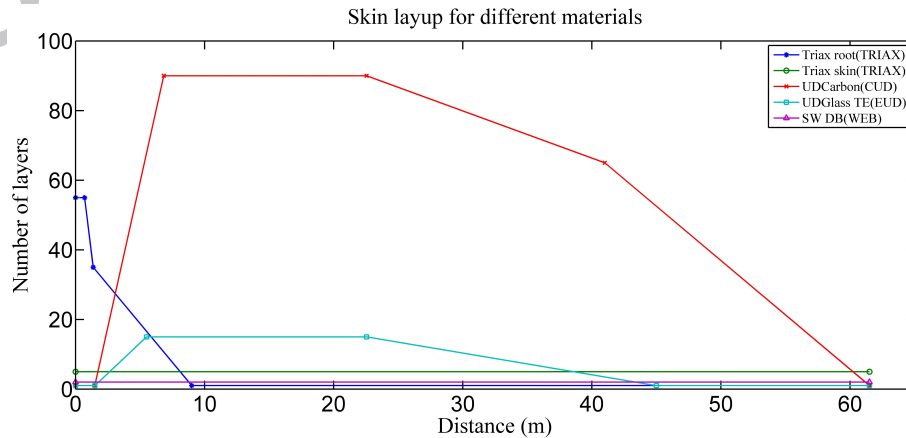


Figure 7: Layup of different composite materials used in the NREL 5MW turbine blade.
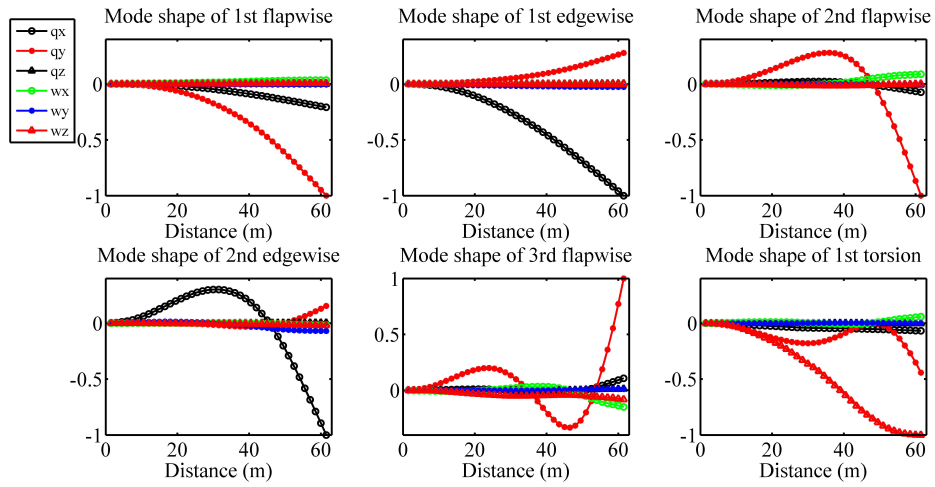
Figure 8: First six mode shapes.



(a) Strain for $0^o$ fibre

(b) Strain for $5^o$ fibre



(c) Strain for $10^o$ fibre

(d) Strain for $15^o$ fibre
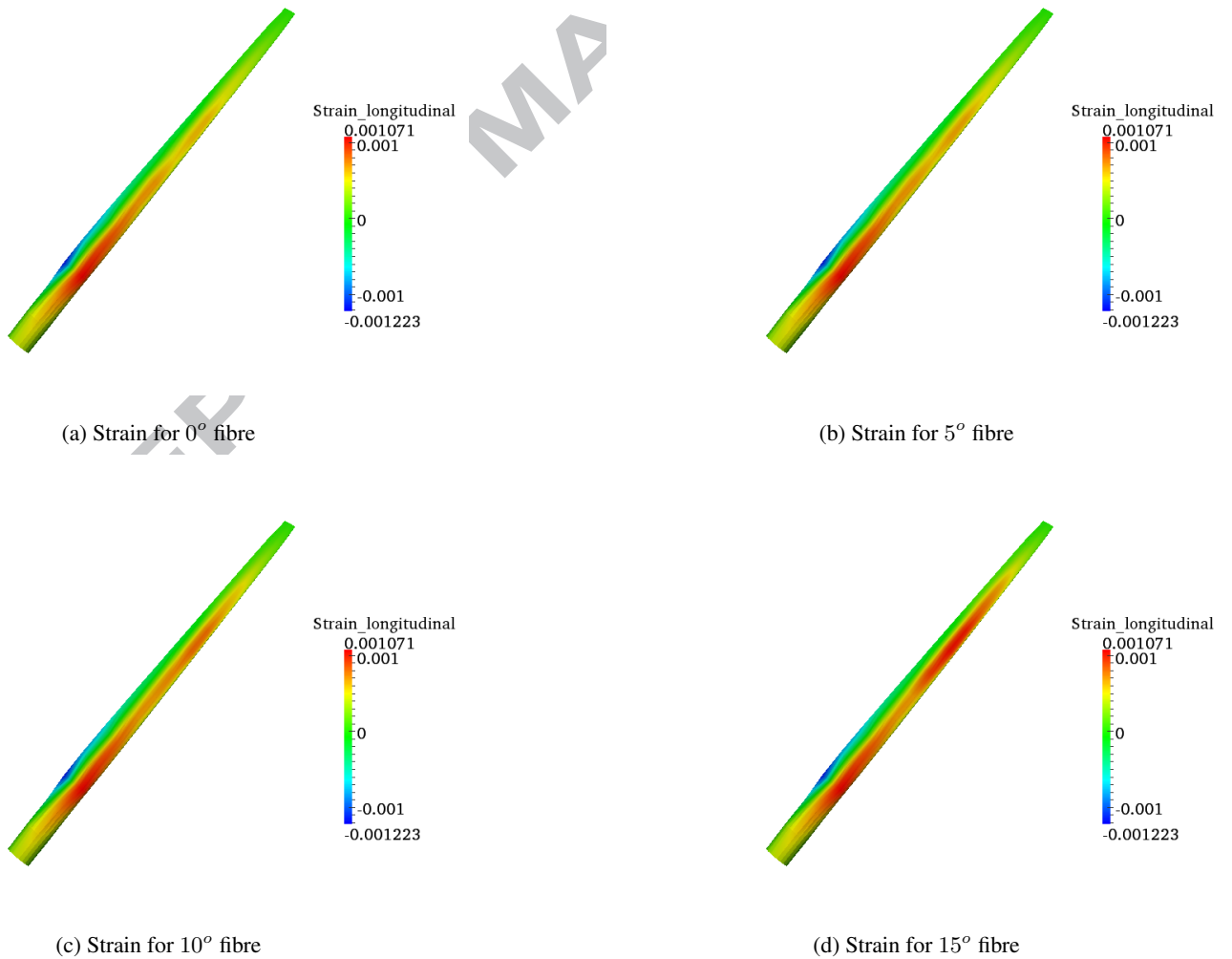
Figure 9: Strain distribution for different orientations (static analysis).

(a) Out-of-plane moment

(b) In-plane moment

(c) Carbon fibre (UD)

(d) Biaxial composite

(e) Glass fibre (UD)

(f) Triaxial composite
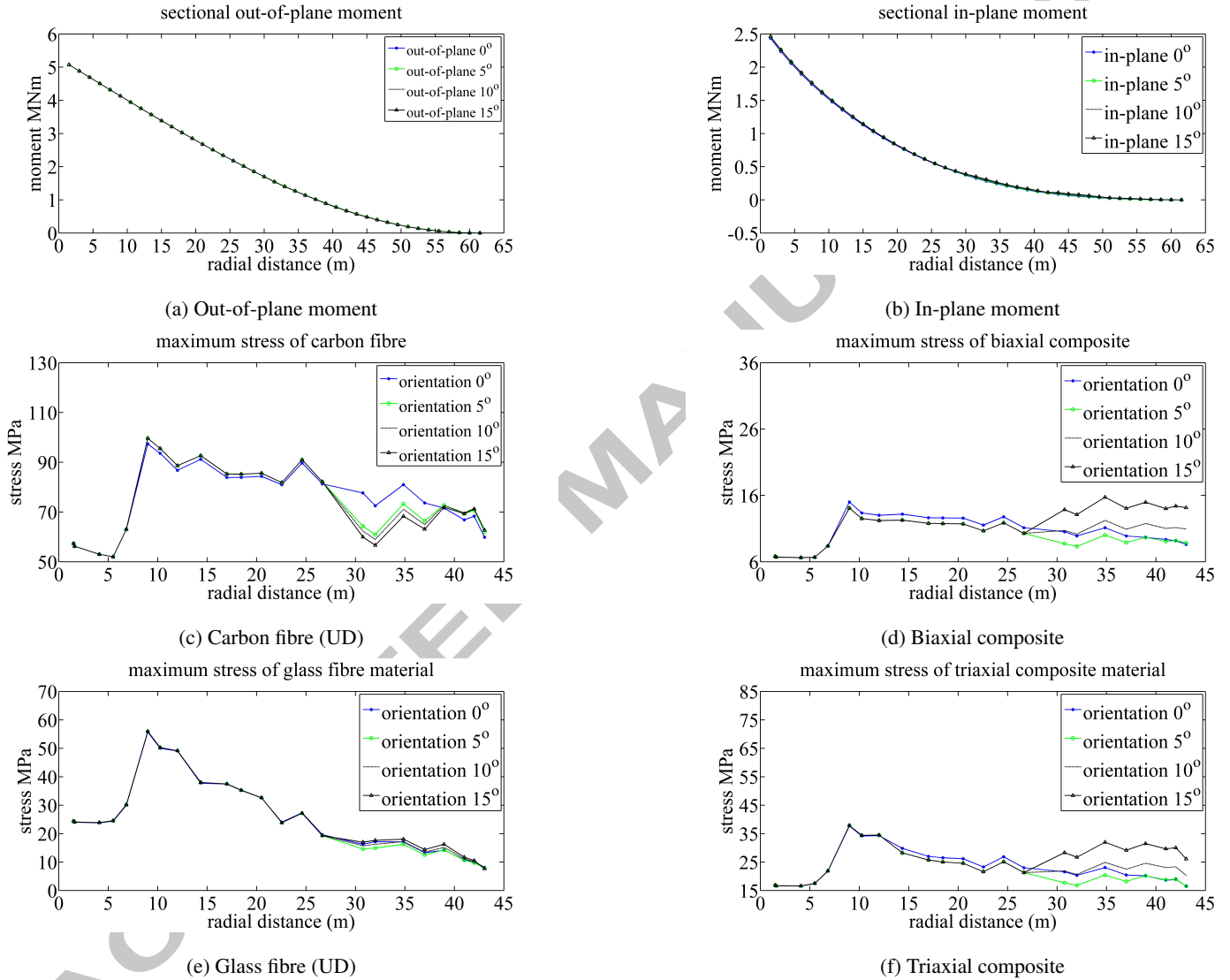
Figure 10: Distributed moment and stress for different materials.
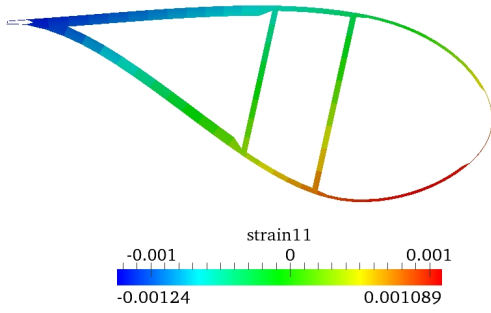
(a) Strain for $0^o$ fibre
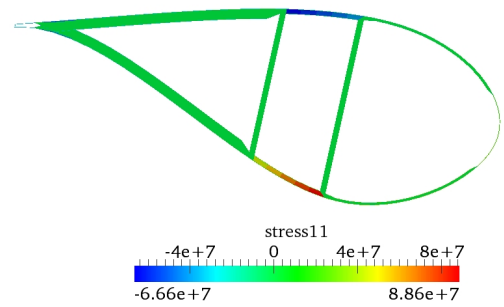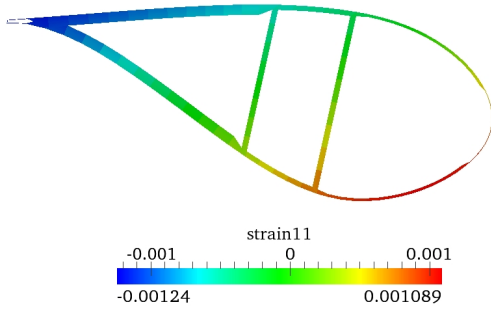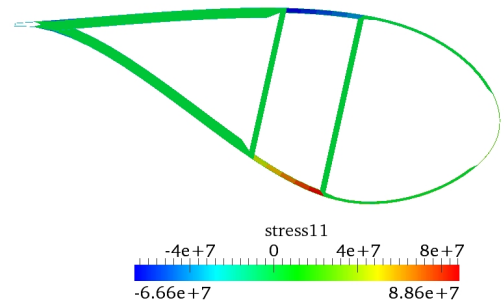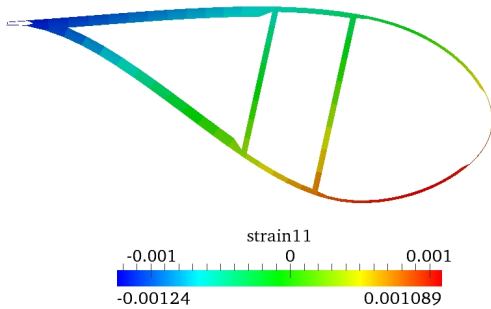


(b) Stress for $0^o$ fibre (Pa)



(c) Strain for $5^o$ fibre



(d) Stress for $5^o$ fibre (Pa)



(e) Strain for $10^o$ fibre
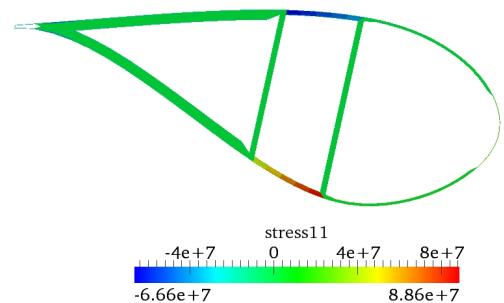


(f) Stress for $10^o$ fibre (Pa)
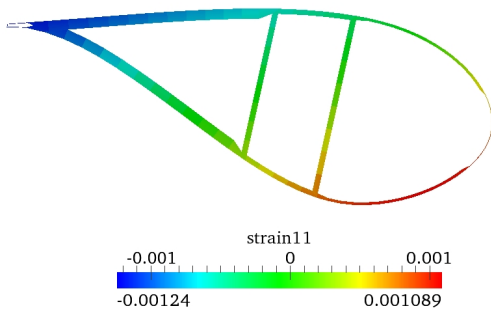


(g) Strain for $15^o$ fibre
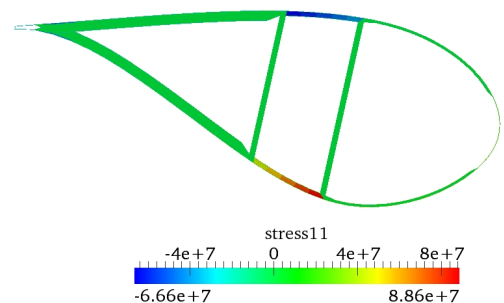


(h) Stress for $15^o$ fibre (Pa)

Figure 11: Longitudinal (fibre-direction) stress and strain isopleths for different fibre orientations on the section 10.25m.
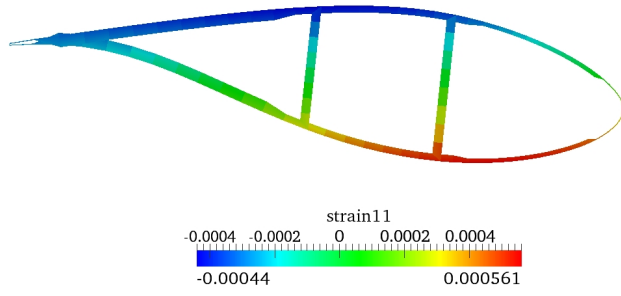
(a) Strain for $0^o$ fibre
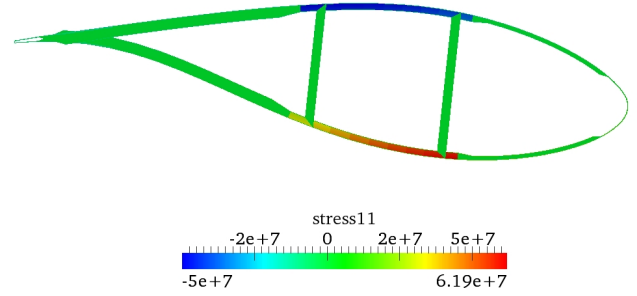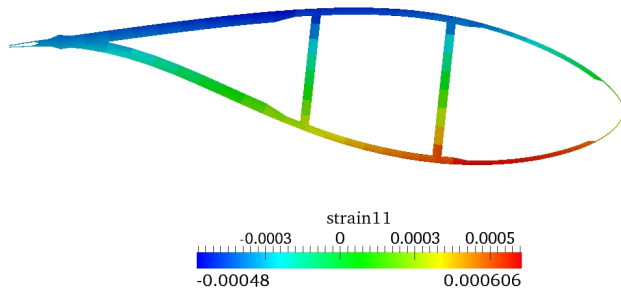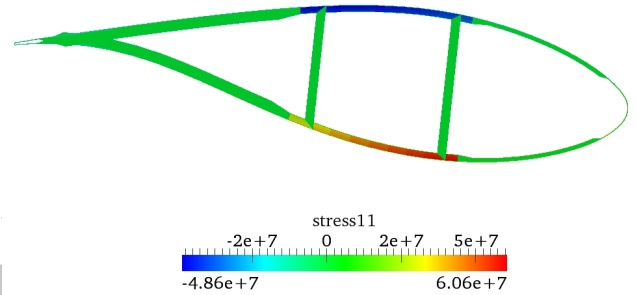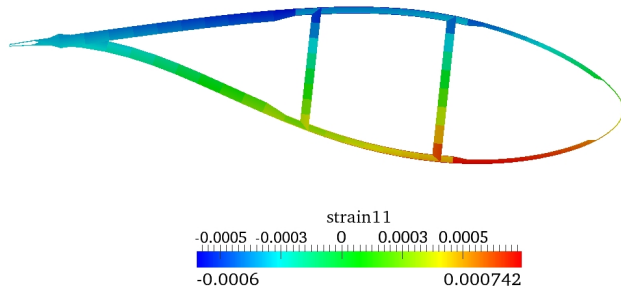


(b) Stress for $0^o$ fibre (Pa)



(c) Strain for $5^o$ fibre



(d) Stress for $5^o$ fibre (Pa)



(e) Strain for $10^o$ fibre
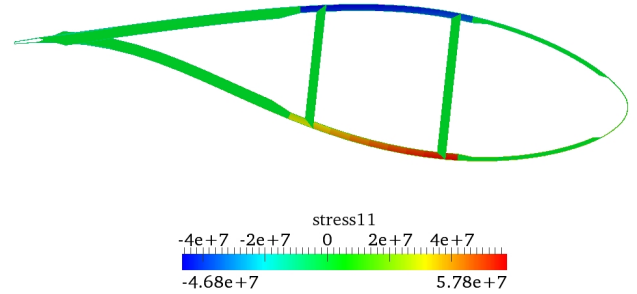


(f) Stress for $10^o$ fibre (Pa)
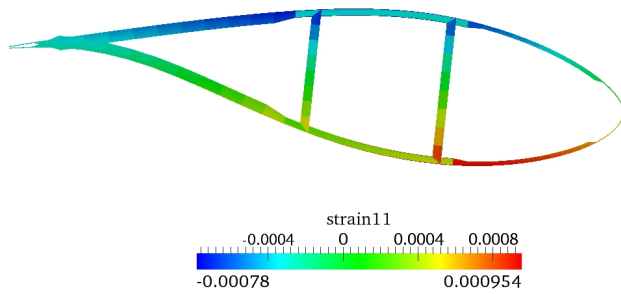


(g) Strain for $15^o$ fibre
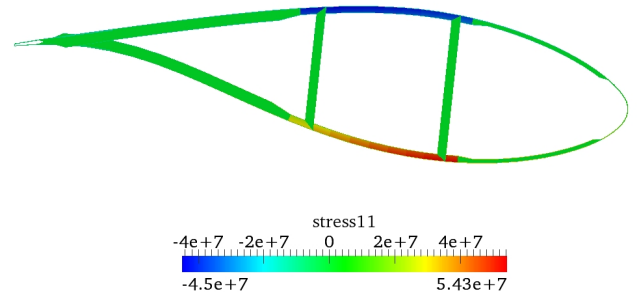


(h) Stress for $15^o$ fibre (Pa)

Figure 12: Longitudinal(fibre-direction) stress and strain isopleths for different fibre orientations on the critical section 30m.

27
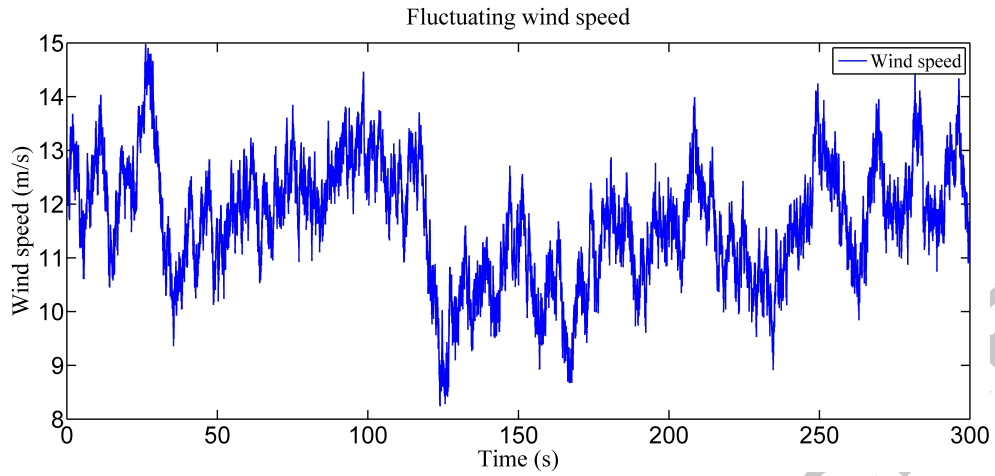
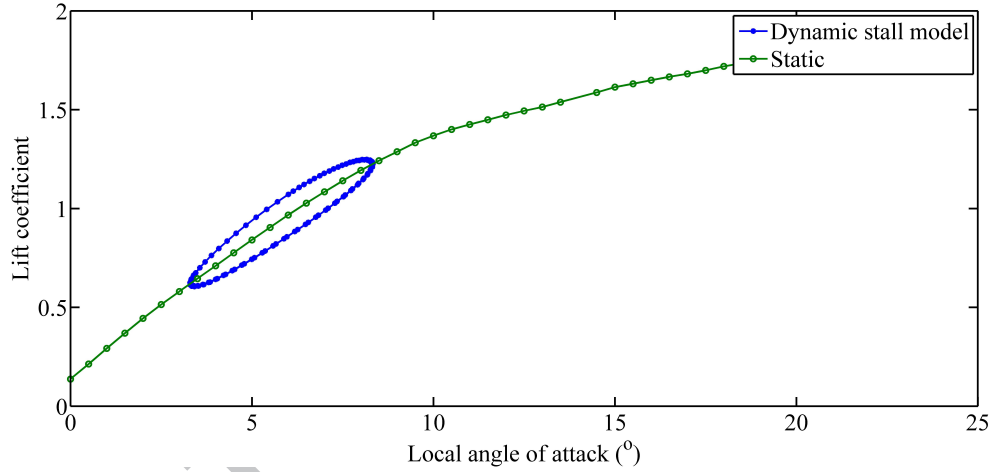Figure 13: Fluctuating longitudinal wind speed under normal wind condition.



Figure 14: Test case 1 for dynamic stall model.
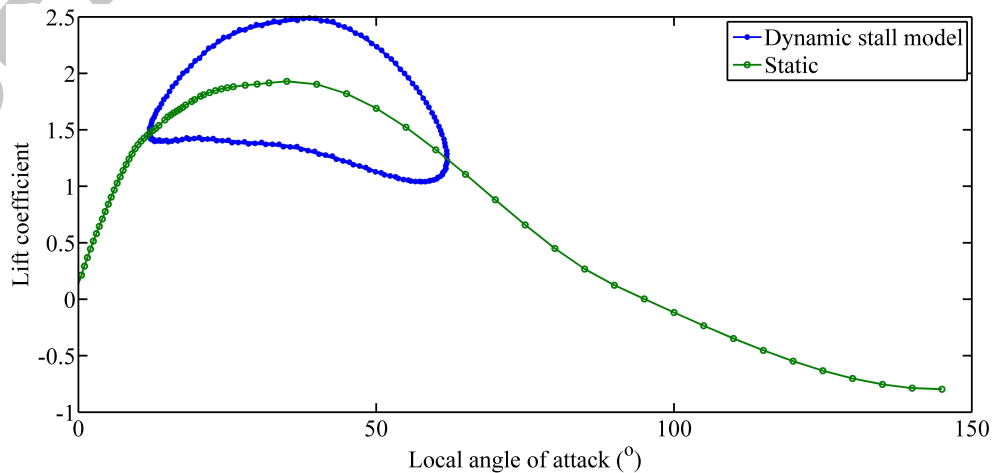


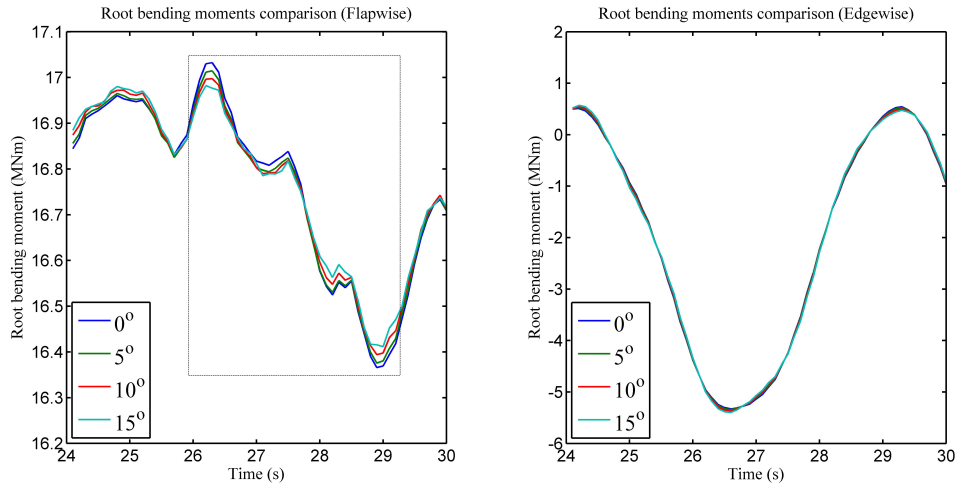Figure 15: Test case 2 for dynamic stall model.

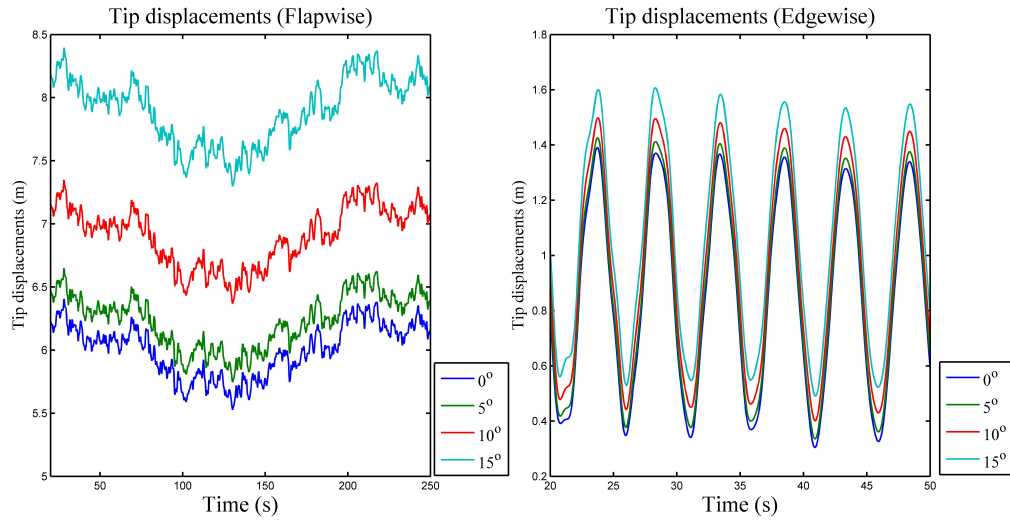Figure 16: Fluctuating root bending moments under the normal wind condition (further enlarged view).



Figure 17: Fluctuating tip displacements under the normal wind condition.
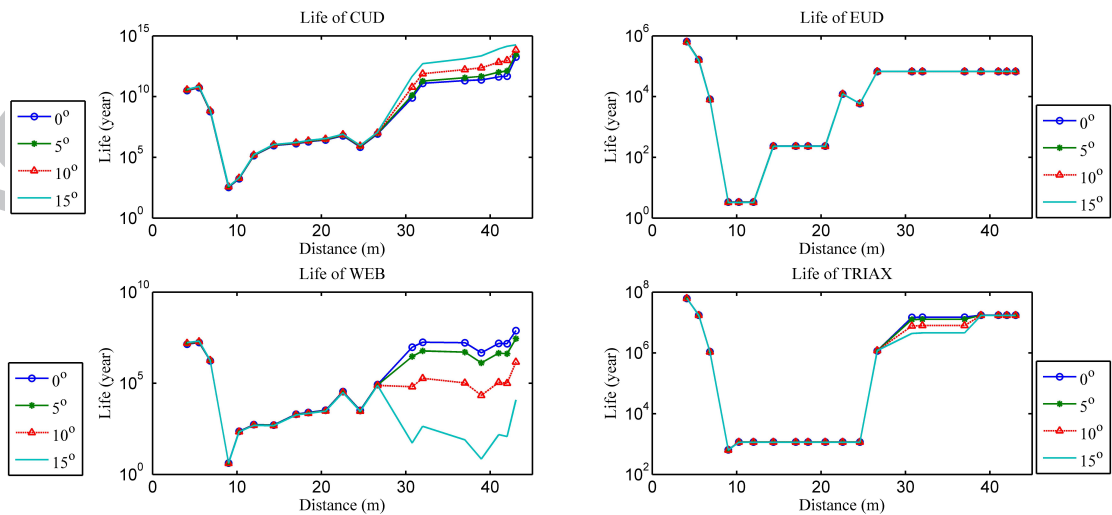


Figure 18: Longevity of different materials on different sections under the normal wind condition.
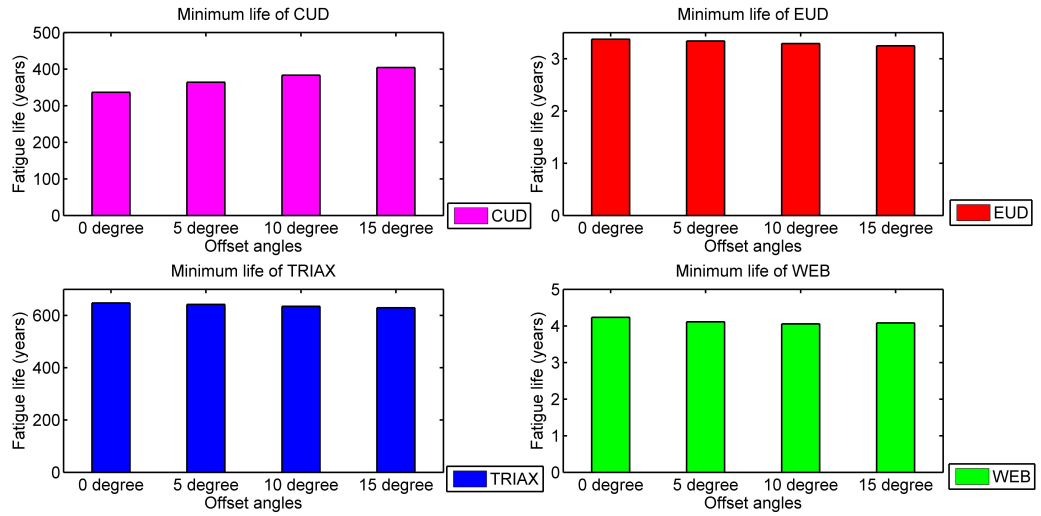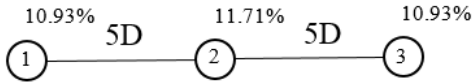
29

Figure 19: Minimum values of longevity of different materials on different sections under the normal wind condition.
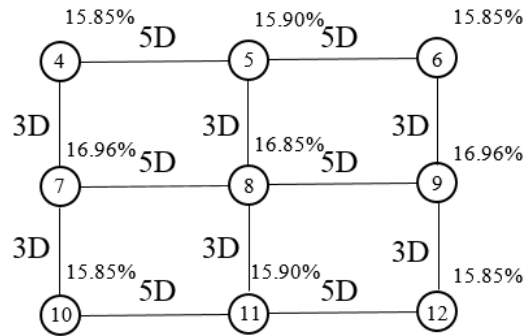


Figure 20: Wind turbine layouts.
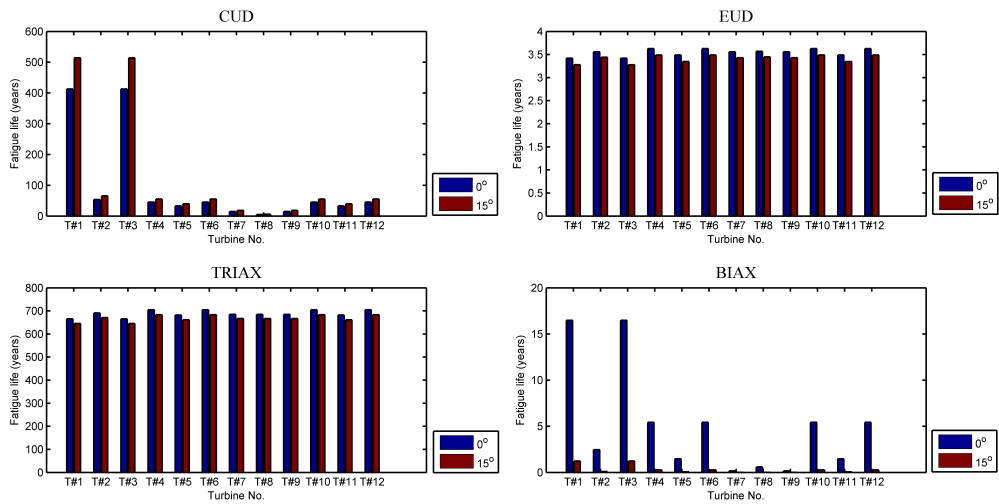


Figure 21: Fatigue life comparison between two different orientations of different wind turbine blades with different materials .

30
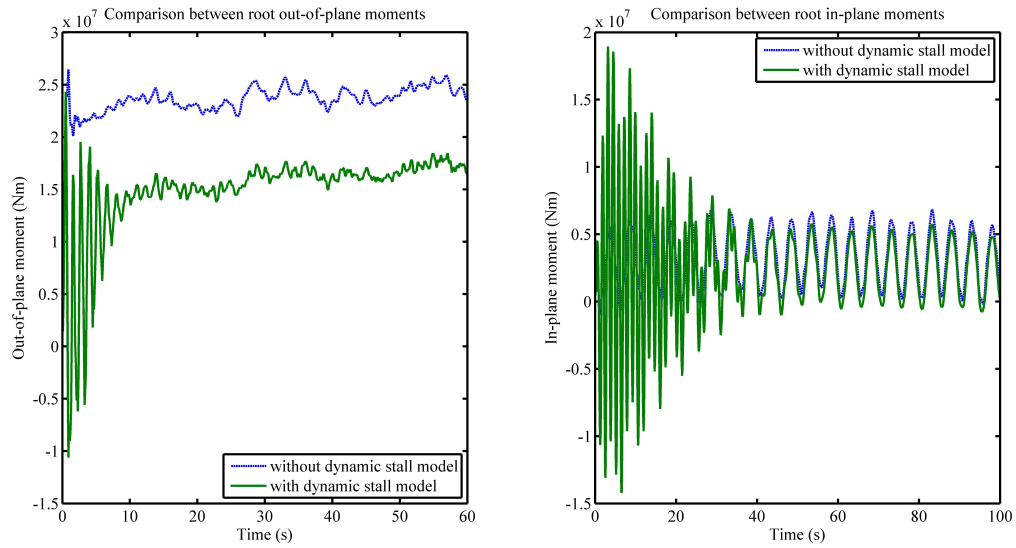
Figure 22: The comparison between the simulated moments of the numerical model with and without dynamic stall model.
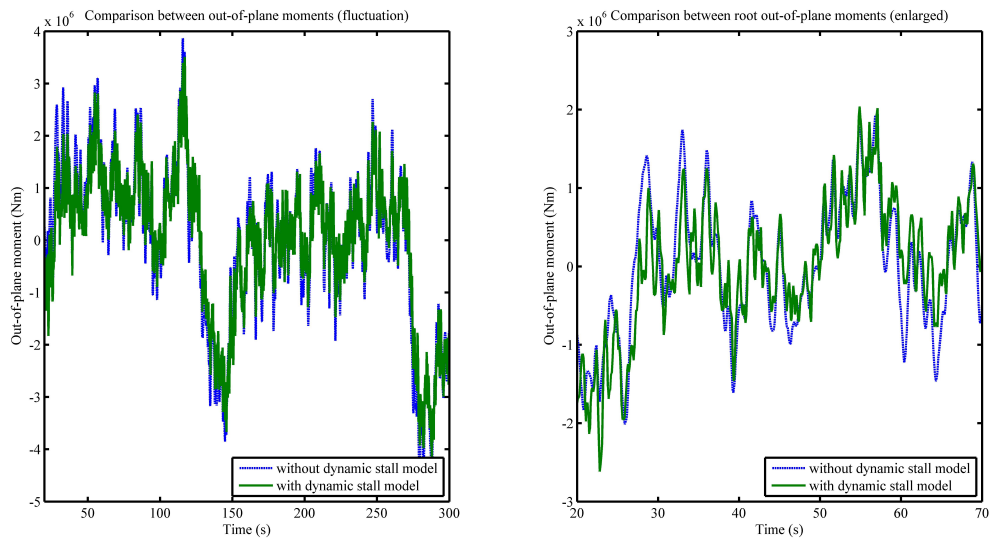


Figure 23: Comparison between the out-of-plane bending moments (with mean value subtracted) with and without dynamic stall model.
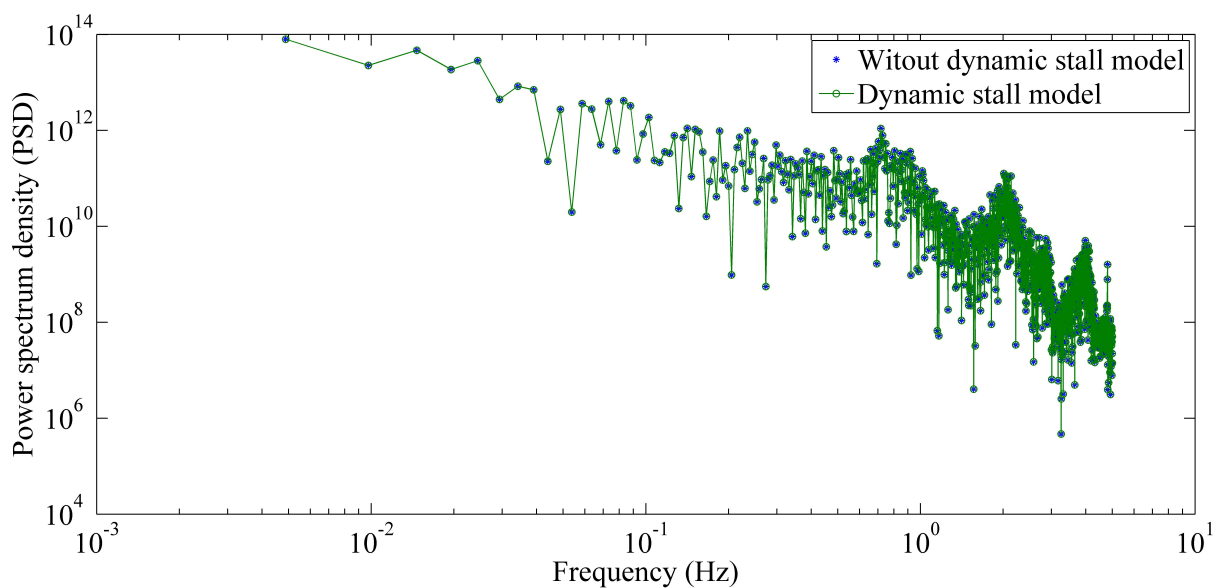
Figure 24: Comparison between the power spectrum of out-of-plane bending moments (with mean value subtracted) with and without dynamic stall model.
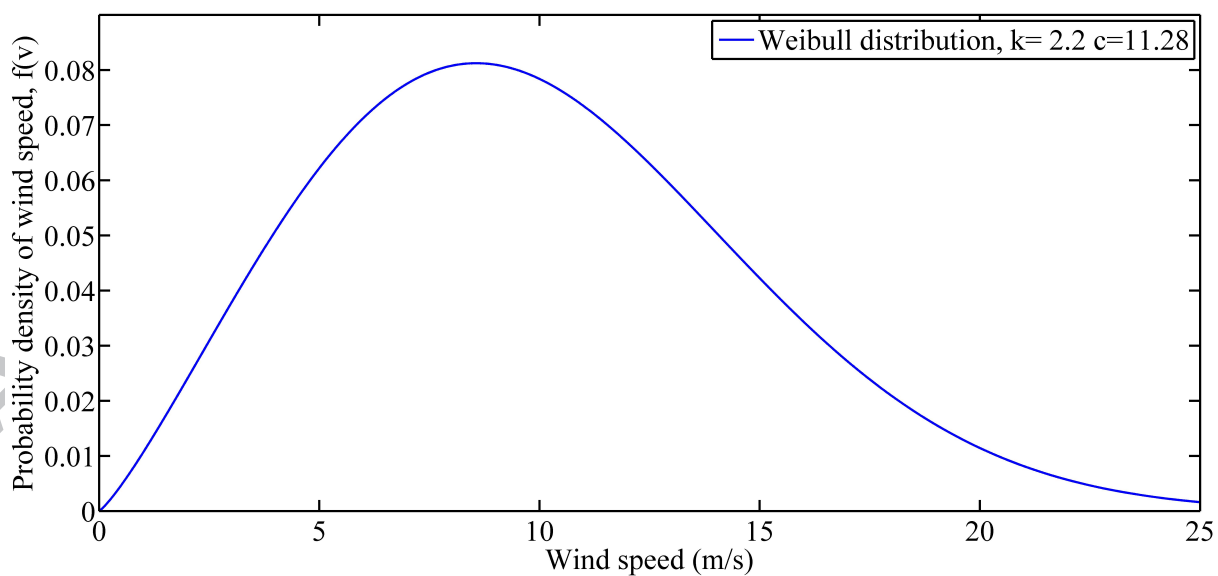


Figure 25: Weibull distribution of wind speed for the simulation case.

Figure 26: Simulated wind speed under no-wake conditions.



Figure 27: Simulated out-of-plane moments under no-wake conditions.

33

Figure 28: Simulated wind speed under wake conditions.
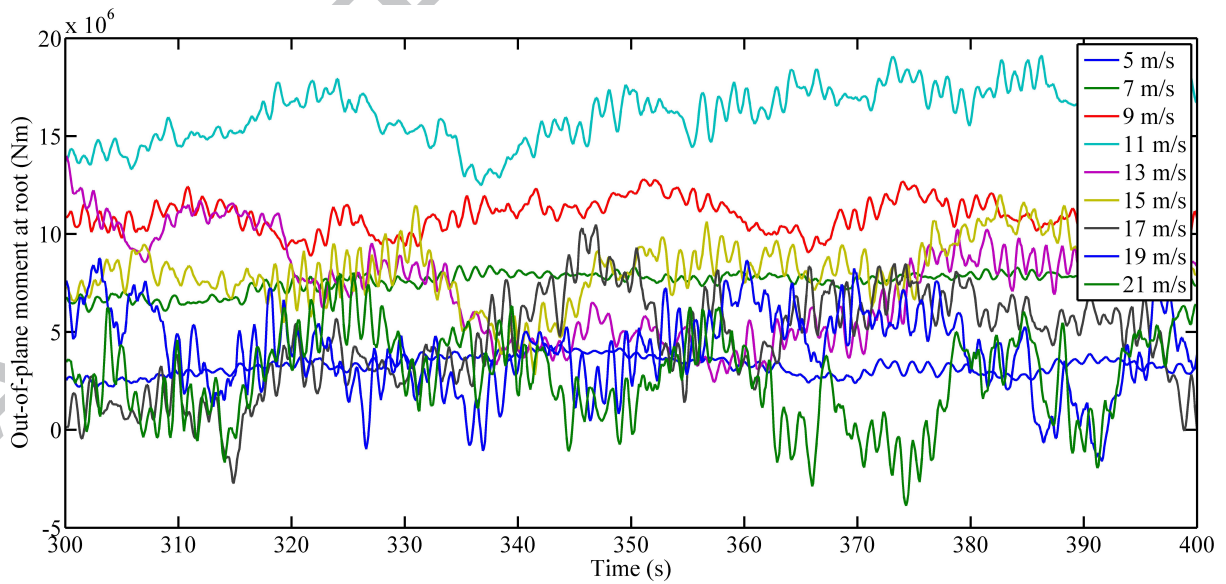


Figure 29: Simulated out-of-plane moments under wake conditions.
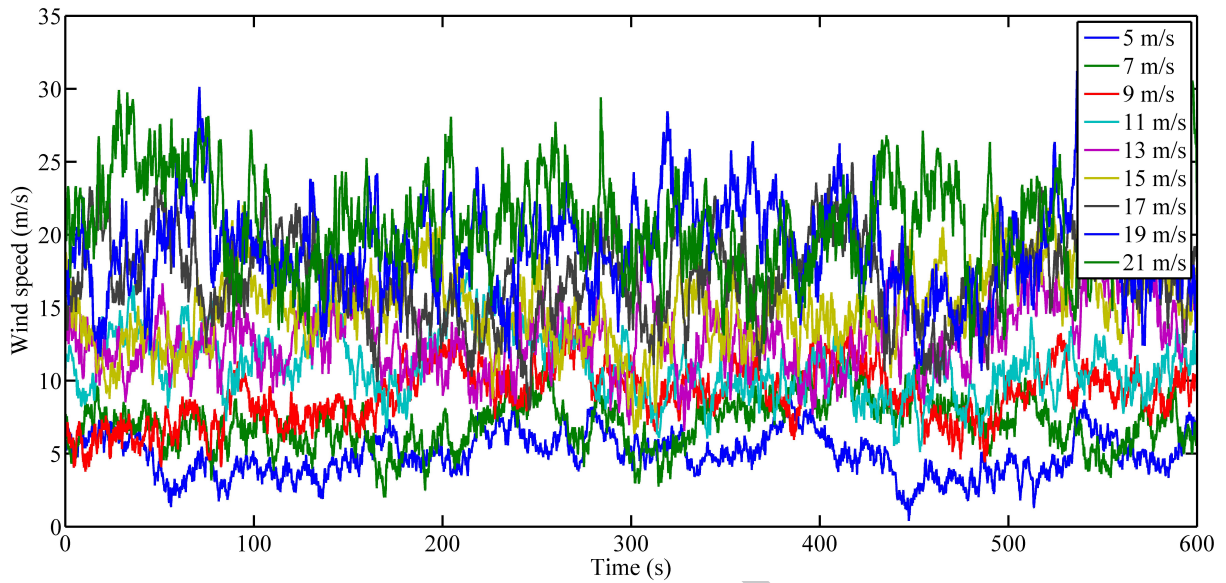
Figure 30: Simulated wind speed under wake conditions and normal layout.
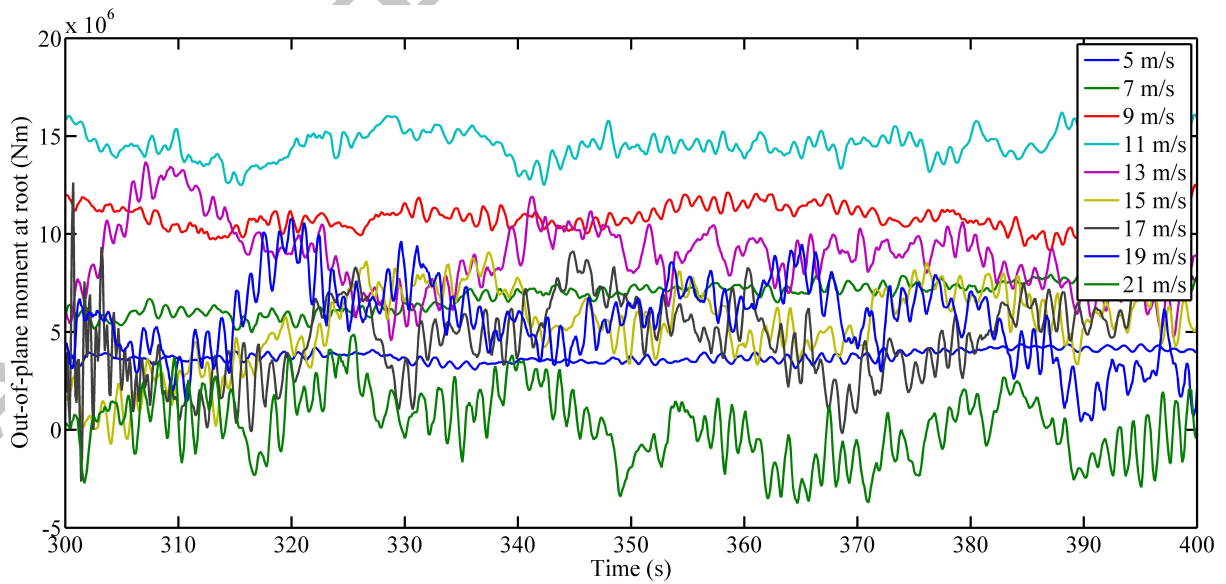


Figure 31: Simulated out-of-plane moments under wake conditions and normal layout.

## 10. Tables

Table 1: Comparison between results obtained with the present beam model and ANSYS in terms of predicted natural frequency.

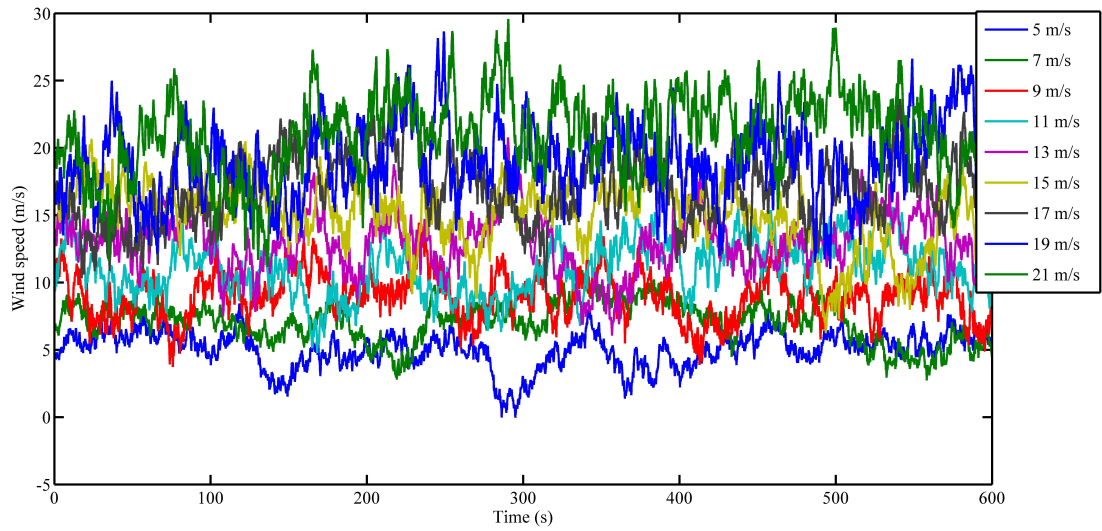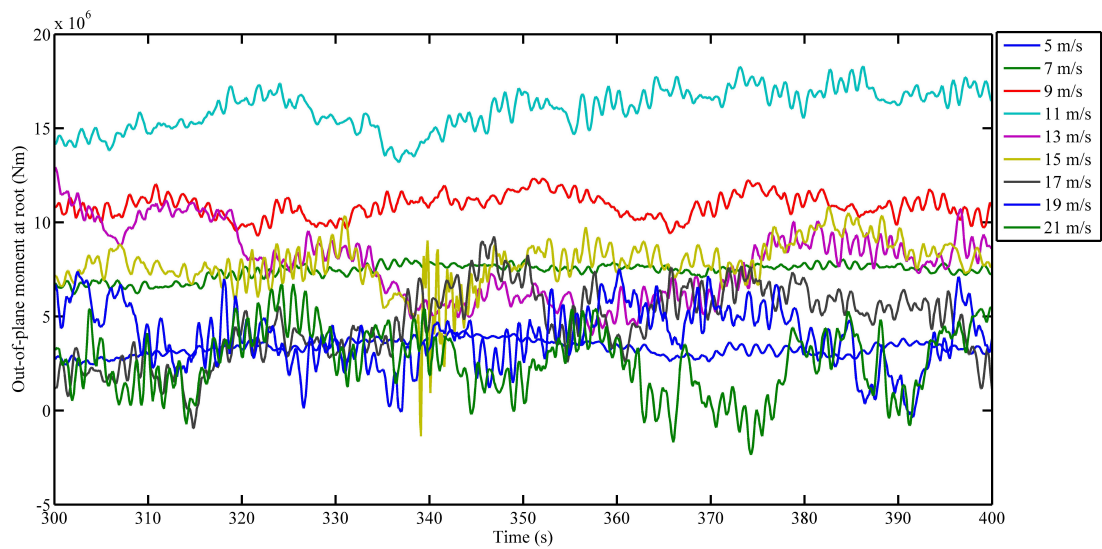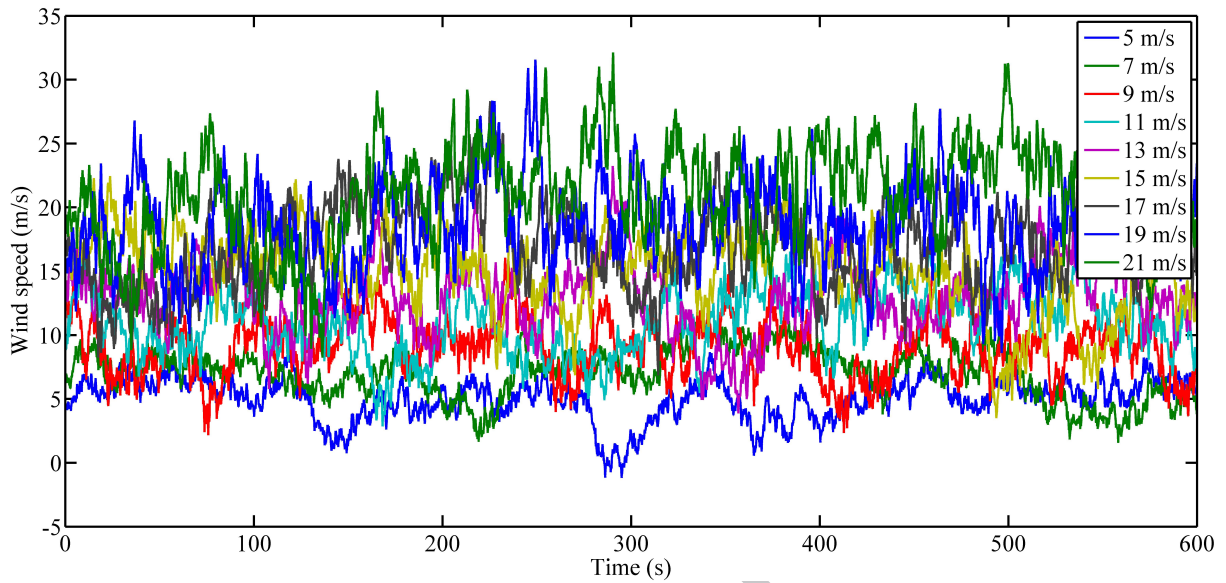| Method | 1st Flapwise (Hz) | 1st Edgewise (Hz) | 2nd Flapwise (Hz) | 2nd Edgewise (Hz) | 3rd Flapwise (Hz) | 1st torsion (Hz) |
|---|---|---|---|---|---|---|
| ANSYS | 0.87 | 1.06 | 2.68 | 3.91 | 5.57 | 6.45 |
| Beam model | 0.89 | 1.04 | 2.72 | 3.90 | 5.75 | 7.15 |

Table 2: The predicted natural frequencies of wind turbine blades with different spar cap orientations.

| Method | 1st Flapwise (Hz) | 1st Edgewise (Hz) | 2nd Flapwise (Hz) | 2nd Edgewise (Hz) | 3rd Flapwise (Hz) | 1st torsion (Hz) |
|---|---|---|---|---|---|---|
| 0 degree | 0.89 | 1.04 | 2.72 | 3.90 | 5.75 | 7.15 |
| 5 degree | 0.88 | 1.04 | 2.63 | 3.87 | 5.72 | 7.16 |
| 10 degree | 0.85 | 1.04 | 2.47 | 3.82 | 5.43 | 7.17 |
| 15 degree | 0.82 | 1.03 | 2.30 | 3.77 | 5.09 | 7.17 |

Table 3: Safety factors for different materials.

| Material | $\gamma_{M_a}$ | $C_{2b}$ | $C_{3b}$ | $C_{4b}$ | $C_{5b}$ | m |
|---|---|---|---|---|---|---|
| Glass fibre | 2.65 | 1.1 | 1.0 | 1.1 | 1.2 | 10 |
| Triaxial fibre | 2.65 | 1.1 | 1.2 | 1.1 | 1.2 | 10 |
| Biaxial fibre | 2.65 | 1.1 | 1.2 | 1.1 | 1.2 | 10 |
| Carbon fibre | 2.65 | 1.1 | 1.0 | 1.1 | 1.2 | 14 |

Table 4: Thickness(each layer) and strength of different materials.

| Material | Thickness (mm) | $\sigma_T$ (MPa) | $\sigma_C$ (MPa) |
|---|---|---|---|
| Glass fibre | 0.47 | 793.05 | -542.49 |
| Triaxial fibre | 0.94 | 700 | -700 |
| Biaxial fibre | 1 | 144 | -213 |
| Carbon fibre | 0.47 | 1546 | -1047 |

Table 5: Parameters for the different wind speed range (from 3 m/s - 25 m/s) under no-wake conditions.

| Wind speed range (m/s) | Characteristic wind speed (m/s) | Rotational speed (rpm) | Pitch angle ($^o$) | Turbulence intensity |
|---|---|---|---|---|
| 3-5 | 5 | 5.31 | 0 | 0.262 |
| 5-7 | 7 | 7.43 | 0 | 0.217 |
| 7-9 | 9 | 9.55 | 0 | 0.192 |
| 9-11 | 11 | 12.1 | 0 | 0.176 |
| 11-13 | 13 | 12.1 | 6.60 | 0.165 |
| 13-15 | 15 | 12.1 | 10.45 | 0.157 |
| 15-17 | 17 | 12.1 | 13.54 | 0.151 |
| 17-19 | 19 | 12.1 | 16.23 | 0.146 |
| 19-21 | 21 | 12.1 | 18.70 | 0.142 |
| 21-23 | 23 | 12.1 | 21.18 | 0.139 |
| 23-25 | 25 | 12.1 | 23.47 | 0.136 |

Table 6: Calculated fatigue life for different materials under no-wake conditions.

| Wind speed range (m/s) | CUD (years) | EUD (years) | TRIAX (years) | BIAX (years) | Weights (Weibull) |
|---|---|---|---|---|---|
| 3-5 | 1.5986e+9 | 53.9377 | 3.7694e+3 | 1.7199e+5 | 0.1377 |
| 5-7 | 2.2980e+7 | 31.1932 | 2.4859e+3 | 1.7459e+5 | 0.1717 |
| 7-9 | 4.3345e+4 | 17.1537 | 1.6062e+3 | 727.5506 | 0.1792 |
| 9-11 | 5.6153 | 9.8457 | 1.1439e+3 | 1.1046 | 0.1627 |
| 11-13 | 15.9887 | 24.0427 | 1.1897e+3 | 5.1545 | 0.1306 |
| 13-15 | 302.7857 | 30.9046 | 963.6181 | 0.4809 | 0.0935 |
| 15-17 | 125.8710 | 21.9941 | 433.0670 | 21.6409 | 0.0600 |
| 17-19 | 100.9939 | 18.0107 | 289.6136 | 7.8679 | 0.0346 |
| 19-21 | 115.6948 | 18.0496 | 208.3771 | 4.7127 | 0.0180 |
| 21-23 | 2.1208e+3 | 13.0352 | 213.2192 | 7.6625 | 0.0084 |
| 23-25 | 3.0045e+3 | 5.2837 | 124.6927 | 1.4742 | 0.0035 |

Table 7: Calculated fatigue life for different materials under no-wake conditions.

| Materials | Fatigue life (years) |
|---|---|
| CUD | 26.0187 |
| EUD | 19.8213 |
| TRIAX | 1.0219e+3 |
| WEB | 2.6190 |

Table 8: Parameters for the different wind speed range (from 3 m/s - 25 m/s) under wake conditions.

| Wind speed range (m/s) | Characteristic wind speed (m/s) | Rotational speed (rpm) | Pitch angle ($^o$) | Turbulence intensity |
|---|---|---|---|---|
| 3-5 | 5 | 5.31 | 0 | 0.321 |
| 5-7 | 7 | 7.43 | 0 | 0.276 |
| 7-9 | 9 | 9.55 | 0 | 0.249 |
| 9-11 | 11 | 12.1 | 0 | 0.230 |
| 11-13 | 13 | 12.1 | 6.60 | 0.217 |
| 13-15 | 15 | 12.1 | 10.45 | 0.206 |
| 15-17 | 17 | 12.1 | 13.54 | 0.198 |
| 17-19 | 19 | 12.1 | 16.23 | 0.190 |
| 19-21 | 21 | 12.1 | 18.70 | 0.184 |
| 21-23 | 23 | 12.1 | 21.18 | 0.179 |
| 23-25 | 25 | 12.1 | 23.47 | 0.174 |

Table 9: Calculated fatigue life for different materials under wake conditions.

| Wind speed range (m/s) | CUD (years) | EUD (years) | TRIAX (years) | BIAX (years) | Weights (Weibull) |
|---|---|---|---|---|---|
| 3-5 | 6.7595e+8 | 53.4924 | 2.7273e+3 | 1.1202e+5 | 0.1377 |
| 5-7 | 6.1500e+6 | 31.1441 | 2.4572e+3 | 5.4080e+5 | 0.1717 |
| 7-9 | 6.5015e+3 | 16.6784 | 1.5444e+3 | 119.7997 | 0.1792 |
| 9-11 | 0.4827 | 9.4055 | 1.0728e+3 | 0.1476 | 0.1627 |
| 11-13 | 0.6079 | 20.0514 | 343.9903e+3 | 0.5905 | 0.1306 |
| 13-15 | 63.8614 | 25.5055 | 725.0841 | 1.0879 | 0.0935 |
| 15-17 | 5.1503 | 12.5421 | 132.5835 | 1.9407 | 0.0600 |
| 17-19 | 4.5651 | 10.0683 | 91.6298 | 1.0541 | 0.0346 |
| 19-21 | 4.4335 | 10.6346 | 34.5358 | 0.7288 | 0.0180 |
| 21-23 | 87.8126 | 6.1392 | 64.8479 | 1.2029 | 0.0084 |
| 23-25 | 168.3429 | 2.0313 | 37.2014 | 0.2011 | 0.0035 |

Table 10: Calculated fatigue life for different materials under wake conditions.

| Materials | Fatigue life (years) |
|---|---|
| CUD | 1.7388 |
| EUD | 16.8524 |
| TRIAX | 406.6164 |
| WEB | 0.6563 |

Table 11: Parameters for the different wind speed range (from 3 m/s - 25 m/s) under wake conditions and normal layout.

| Materials | Characteristic wind speed (m/s) | Rotational speed (rpm) | Pitch angle ($^o$) | Turbulence intensity |
|---|---|---|---|---|
| 3-5 | 5 | 5.31 | 0 | 0.2911 |
| 5-7 | 7 | 7.43 | 0 | 0.2450 |
| 7-9 | 9 | 9.55 | 0 | 0.2183 |
| 9-11 | 11 | 12.1 | 0 | 0.2006 |
| 11-13 | 13 | 12.1 | 6.60 | 0.1879 |
| 13-15 | 15 | 12.1 | 10.45 | 0.1784 |
| 15-17 | 17 | 12.1 | 13.54 | 0.1710 |
| 17-19 | 19 | 12.1 | 16.23 | 0.1648 |
| 19-21 | 21 | 12.1 | 18.70 | 0.1596 |
| 21-23 | 23 | 12.1 | 21.18 | 0.1556 |
| 23-25 | 25 | 12.1 | 23.47 | 0.1517 |

Table 12: Calculated fatigue life for different materials under wake conditions and normal layout for normal blade.

| Wind speed range (m/s) | CUD (years) | EUD (years) | TRIAX (years) | BIAX (years) | Weights (Weibull) |
|---|---|---|---|---|---|
| 3-5 | 2.0312e+9 | 51.0607 | 3.5647e+3 | 1.9869e+5 | 0.1377 |
| 5-7 | 9.9102e+6 | 30.8361 | 2.4187e+3 | 9.1604e+4 | 0.1717 |
| 7-9 | 2.8041e+4 | 17.1227 | 1.5980e+3 | 739.0295 | 0.1792 |
| 9-11 | 1.2108 | 9.6709 | 1.1171e+3 | 0.3079 | 0.1627 |
| 11-13 | 21.0242 | 22.4947 | 1.0453e+3 | 2.7883 | 0.1306 |
| 13-15 | 39.9979 | 25.9339 | 697.1048 | 4.9734 | 0.0935 |
| 15-17 | 143.2279 | 25.5949 | 530.6142 | 3.2463 | 0.0600 |
| 17-19 | 44.4458 | 15.2231 | 219.5617 | 2.3996 | 0.0346 |
| 19-21 | 229.5693 | 11.9032 | 247.8988 | 7.3153 | 0.0180 |
| 21-23 | 88.3748 | 8.7207 | 118.7112 | 2.2269 | 0.0084 |
| 23-25 | 7.6653 | 4.1704 | 34.3980 | 1.1356 | 0.0035 |

Table 13: Calculated fatigue life for different materials under wake conditions and normal layout for normal blade.

| Materials | Fatigue life (years) |
|---|---|
| CUD | 6.9084 |
| EUD | 18.7893 |
| TRIAX | 874.4315 |
| WEB | 1.5712 |

Table 14: Calculated fatigue life for different materials under wake conditions and normal layout for BTC blade.

| Wind speed range (m/s) | CUD (years) | EUD (years) | TRIAX (years) | BIAX (years) | Weights (Weibull) |
|---|---|---|---|---|---|
| 3-5 | 2.7593e+9 | 54.9027 | 3.8601e+3 | 2.3339e+5 | 0.1377 |
| 5-7 | 1.4935e+7 | 29.0696 | 2.3079e+3 | 9.3524e+4 | 0.1717 |
| 7-9 | 2.7796e+4 | 16.5784 | 1.5452e+3 | 834.5782 | 0.1792 |
| 9-11 | 1.1838 | 9.5579 | 1.1099e+3 | 0.3079 | 0.3466 |
| 11-13 | 42.1325 | 22.2240 | 1.0443e+3 | 2.7883 | 3.8398 |
| 13-15 | 45.3534 | 21.2948 | 575.2739 | 4.9734 | 6.1749 |
| 15-17 | 507.0271 | 17.5519 | 385.7082 | 3.2463 | 3.4022 |
| 17-19 | 104.3946 | 13.8084 | 192.5606 | 2.3996 | 12.2359 |
| 19-21 | 359.1663 | 8.7844 | 178.3102 | 7.3153 | 9.8222 |
| 21-23 | 69.3830 | 4.8082 | 62.2503 | 2.2269 | 1.4874 |
| 23-25 | 5.8628 | 2.4603 | 20.5534 | 1.1356 | 0.6109 |

Table 15: Calculated fatigue life for different materials under wake conditions and normal layout for BTC blade.

| Materials | Fatigue life (years) |
|---|---|
| CUD | 6.9532 |
| EUD | 17.3377 |
| TRIAX | 712.3523 |
| WEB | 1.8097 |

Table 16: Parameters of dynamic stall model.

| Parameters | Values |
|---|---|
| $\omega_1$ | 0.0455 |
| $\omega_2$ | 0.3 |
| $\omega_3$ | 0.0875 |
| $\omega_4$ | 0.4125 |
| $A_1$ | 0.165 |
| $A_2$ | 0.335 |